Palaeogeography, Palaeoclimatology, Palaeoecology 637 (2024) 111995

Contents lists available at ScienceDirect

Palaeogeography, Palaeoclimatology, Palaeoecology

journal homepage: www.elsevier.com/locate/palaeo

Late Cretaceous (Cenomanian-Turonian) temperature evolution and biotic response in the Adriatic Carbonate Platform region of Friuli, northeast Italy

B. Křížová [a], L. Consorti [b], S. Cardelli [a], K.E. Schmitt [c], V. Brombin [a], M. Franceschi [d], G. Tunis [e], L. Bonini [d], G. Frijia [a,*]

[a] Depatrment of Physics and Earth Sciences, University of Ferrara, via Saragat 1, 44121 Ferrara, Italy
[b] Institute of Marine Sciences (ISMAR-CNR), Area Science Park, Basovizza, 34149 Trieste, Italy
[c] Institute of Geosciences, University of Mainz, Johann-Joachim-Becher-Weg 21, 55128 Mainz, Germany
[d] Department of Mathematics and Geosciences, University of Trieste, Via Weiss 2, 34128 Trieste, Italy
[e] University of Trieste, Via Margotti 19, 34170 Gorizia, Italy

ARTICLE INFO

Editor: H Falcon-Lang

Keywords:
Cretaceous Paleotemperatures
Carbonate Platforms
Chemostratigraphy
Benthic
Foraminifera
Rudist bivalves

ABSTRACT

Climate modelling and palaeotemperature reconstructions derived from several proxies (TEX_{86}, $\delta^{18}O$) suggest that the Late Cretaceous was one of the warmest intervals in Earth history. The greenhouse climate reached its acme near the Cenomanian-Turonian boundary (CTB) interval with sea surface temperatures over 35 °C in low and mid- palaeolatitudes, coinciding with the highest sea level stands of the Phanerozoic. Following this warming phase, a general cooling trend punctuated by short-term hot snaps characterized the rest of the Cretaceous. Palaeotemperature and palaeoenvironmental changes are well documented in deep-water carbonate deposits based on variations in geochemical proxies and distribution patterns of macro- and microfauna. However, such climatic and environmental fluctuations severely impacted carbonate platforms, sedimentary environments that are particularly sensitive to external perturbations. Palaeontological data show major changes within the main carbonate platform producers (rudists and benthic foraminifera) during the early Late Cretaceous. Both groups experienced major taxonomic turnovers at the CTB, followed by a further re-radiation in the middle/late Turonian. The lack of detailed palaeoclimatic reconstructions in shallow water carbonate succession hampers the possibility to investigate a possible causal relationship between temperature changes and faunal evolution. In this paper, we report integrated geochemical, sedimentological, and palaeontological data from the Adriatic Carbonate Platform (Friuli, north-east Italy). Benthic foraminifera biostratigraphy and isotope stratigraphy ($\delta^{13}C$ and $^{87}Sr/^{86}Sr$) were used to precisely constrain the stratigraphy of the late Cenomanian-middle Turonian interval. $\delta^{18}O$ analysis on both well-preserved rudist shells and bulk rock samples enabled the construction of high-resolution palaeotemperature curves. The resulting temperature trends are comparable with those from the deep-water record across the late Cenomanian-Turonian interval. The warmest phase was in the Early Turonian with sea surface palaeotemperatures as high as 41–45 °C recorded in rudist shells. Data show temperature fluctuation from the late Cenomanian to the Early Turonian with a magnitude >7 °C. Benthic foraminifera and rudist evolution responded to these palaeotemperature fluctuations, and their decline in the late Cenomanian and full recovery in the Turonian suggest a strong link with temperature changes.

1. Introduction

The Late Cretaceous was characterized by extremely high temperatures in the oceans and continents. The modelled CO_2 concentration in the atmosphere was among the highest of the entire Phanerozoic (e.g., Bice et al., 2006; Burgener et al., 2023; Hay and Floegel, 2012; O'Brien et al., 2017), and has been considered as the main driver of the warm Cretaceous climate (e.g., Hay and Floegel, 2012). Numerous studies evidenced a reduced equator-to-pole temperature gradient during the Late Cretaceous (Hay, 2008; O'Connor et al., 2019 among others), while the presence of latitudinal variations similar to the modern ones has also been proposed (de Winter et al., 2021; Pucéat et al., 2007). A gradual warming started in the Albian and culminated during the Cretaceous Thermal Maximum (KTM) in the late Cenomanian and Early Turonian

* Corresponding author.
E-mail address: gianluca.frijia@unife.it (G. Frijia).

https://doi.org/10.1016/j.palaeo.2023.111995
Received 17 April 2023; Received in revised form 19 December 2023; Accepted 19 December 2023
Available online 22 December 2023

(O'Brien et al., 2017), where sea-surface temperatures (SSTs) reached ≥30 °C in the tropics and ≥ 20 °C in the southern mid-to-high latitudes (Friedrich et al., 2012; Huber et al., 2018; O'Brien et al., 2017; Scotese et al., 2021; Song et al., 2019). A few studies suggested possible glacial episodes during the middle Turonian (Bornemann et al., 2008; Galeotti et al., 2009; Miller et al., 2004), but this theory has been recently questioned by high-resolution SST reconstructions showing extreme warmth during the whole Turonian, even at high latitudes (Huber et al., 2018; MacLeod et al., 2013; O'Connor et al., 2019). Concurrently, the sea level rose to its Cretaceous maximum (Haq, 2014; Miller et al., 2004), flooding large portions of continental margins and creating shallow water environments suitable for carbonate platform establishment (Pohl et al., 2019). The KTM was followed by a long-term gradual cooling which lasted until the Maastrichtian (Clarke and Jenkyns, 1999; Friedrich et al., 2012; O'Brien et al., 2017; O'Connor et al., 2019; Steuber et al., 2005a). Even though the Cretaceous climate is among those better studied in the geological past, mechanisms and forcing factors of heat transfer in the different ocean settings are still unclear. Most Cretaceous palaeoclimatological studies are based on the $\delta^{18}O$ analysis of bulk rock and foraminifera from deep-water carbonate successions (e.g. Clarke and Jenkyns, 1999; Friedrich et al., 2012; Huber et al., 2002, 2018; Petrizzo et al., 2022), or use organic geochemical palaeothermometer TEX_{86} (e.g., O'Brien et al., 2017; O'Connor et al., 2019). Neritic carbonate successions, despite being important archives of climate and environmental changes, have been largely overlooked. Thus, considering the extensive presence of shallow water carbonate environments in the Late Cretaceous world, this represents a major gap in understanding the Late Cretaceous climate and biota evolution.

The limited studies on Cretaceous climatic reconstructions from neritic settings are mainly based on rudist bivalves, the major macro-calcifiers in the Late Cretaceous shallow seas, (Steuber et al., 2005a; Huck and Heimhofer, 2021). During the Late Cretaceous, rudist bivalves as well as other important shallow-marine calcifying organisms such as benthic foraminifera experienced episodes of demise and extinctions (Steuber, 2003; Parente et al., 2008; Steuber et al., 2023). However, it is still unclear whether temperature variations had a role in impacting neritic faunas or acted in connection with other environmental perturbations associated with the oceanic anoxic events (OAEs; Steuber et al., 2023). Recent data suggest that the majority of the extinction events during the Phanerozoic coincided with extreme warming or cooling phases (Song et al., 2021). Therefore, understanding seasonal temperature variability, latitudinal temperature gradients, and absolute temperatures in neritic settings would help to elucidate the mechanisms of heat transfer, ocean circulation, and the response of biota to temperature perturbations. High-resolution intra-shell sampling of rudist shells from different locations has permitted estimation of seasonal variability during the Cretaceous (de Winter et al., 2021; Huck and Heimhofer, 2021; Steuber et al., 2005a; Walliser and Schöne, 2020; Schmitt et al., 2022) thereby contributing to a better understanding of the oceanic heat transfer dynamics. These researches have, however, focused on low-resolution compilation of isotopic data from rudists of different ages and locations thus hampering a precise correlation between temperature changes and biota evolution.

This study provides high-resolution palaeotemperature reconstruction based on $\delta^{18}O$ analysis of bulk-rock data and well-preserved rudists through an expanded Cenomanian-Turonian shallow-water carbonate section cropping out in the Friuli region (Italy). Facies analysis and sedimentological observations were used to reconstruct biota evolution and depositional settings. Biostratigraphy and isotope stratigraphy ($\delta^{13}C$ and $^{87}Sr/^{86}Sr$) allowed for building a precise chronostratigraphic framework. Palaeotemperature trends and absolute estimates were compared with published deep-water and shallow-water data to evaluate local vs. global signatures. Finally, the reconstructed temperatures were correlated with rudists and benthic foraminifera distribution to highlight possible causal relationships.

2. Geological setting

The studied section (near the village of Devetachi) is located along a road cut of the SS n. 47 between Trieste and Gorizia (45.86 N, 13.57 E) and belongs to the so-called Friuli Carbonate Platform (FCP). This carbonate platform was situated at the NW corner of the larger Adriatic Carbonate Platform (AdCP), which was part of a Mesozoic archipelago of isolated carbonate shelves bordered by pelagic and/or hemipelagic basins (Sanders, 2001; Vlahović et al., 2005). Mesozoic and Palaeocene shallow-water carbonate deposits of the FCP are overlain by a Middle Eocene siliciclastic succession of flysch, in some localities containing large carbonate olistoliths. The geological setting is the result of the Dinaric and Alpine orogeny, starting with the Late Cretaceous forebulging which continued through the Palaeocene, until the Middle Eocene, when the advancement of the Dinaric chain is testified by siliciclastic deposits of the flysch succession (Otoničar, 2007). Devetachi section is part of the "Aurisina limestone" unit (upper Cenomanian to Lower Campanian according to Consorti et al., 2021). Its lower part includes the Cenomanian-Turonian transition (Fig. 1), similar to other records reported in the surroundings of the study area (Melis et al., 2000).

3. Material and methods

The studied section is almost 150 m thick. Extensive fieldwork and close-spaced sampling (mostly up to 50 cm and not exceeding 1 m) were performed for lithological, sedimentological, biostratigraphic, and geochemical analyses. Over 100 thin sections were studied.

The abundance of rudists and rudist beds was estimated assuming that these parameters mirror the productivity of rudist communities (see Frijia et al., 2014). The relative richness in rudists within a single bed was considered as well as the thickness of rudist beds, and the spacing between these individual beds. We distinguished three scenarios: 1) Absent, no rudist beds over a stratigraphic interval of at least 10 m; 2) Scarce: rudist beds 20–60 cm thick and 2–8 m apart, wackestone-packstone with sparse shell fragments, more rarely floatstone with small shells (max diameter 3–4 cm), 3) Abundant: rudist beds 40–170 cm thick and 4 cm to 4 m (rarely 6 m) apart, rudist floatstone or rudstone with densely packed shells up to 15–20 cm long and 4–8 cm in diameter.

For geochemical purposes, all samples were cleaned, cut, polished, and microdrilled. $\delta^{13}C$ and $\delta^{18}O$ analyses were performed at the Paleoclimatology and isotope stratigraphy lab of the University of Ferrara. 285 samples of bulk rock and 133 samples of rudists and 2 *Chondrodonta* fragments were analyzed using isoFLOW (Elementar©) operating in continuous flow with a PrecisION IRMS (Elementar©). The external precision for the isoFLOW is 0.08 ‰. Analytical uncertainties (1 sigma) for the isotope analyses were in the order of ±0.1 ‰ for $\delta^{13}C$ and $\delta^{18}O$. The $^{13}C/^{12}C$ and $^{18}O/^{16}O$ isotopic ratios are expressed in the δ notation (in ‰ units) relative to VPDB. Further details on $\delta^{13}C$ and $\delta^{18}O$ geochemical analyses are reported in the Supplementary material.

22 samples of rudists (19 radiolitids and 3 requinids) were selected for Sr-isotope stratigraphy (SIS). The analytical procedure followed that described in Mueller et al. (2020): powdered samples containing ca 400 ng of Sr were dissolved first in 1 ml of 6 M HCl for about 24 h and then, after drying, in 0.4 ml of 3 M HNO_3. The Sr fraction was separated from the matrix using PFA columns filled with TRISKEM ion exchange resin and re-dissolved in 1 ml of H2O2-HNO3 (1:1) to remove organic remains and then dried. Finally, samples were re-dissolved in 1 μl of ionization-enhancing solution and loaded on Re single filaments. The loading, column, and reagent blanks were < 5 pg, <1 ng, and < 0_01 ppb, respectively. The $^{87}Sr/^{86}Sr$ ratios were analyzed on a Thermal Ionization Mass Spectrometer (TIMS) TI-Box (formerly MAT 262; company – Spectromat, Bremen, Germany) spectrometer and normalized to an $^{87}Sr/^{86}Sr$ value of 0.1194. Long-term reproducibility was determined using the reference materials NIST NBS 987 and USGS EN-1 and resulted in an $^{87}Sr/86^{Sr}$ ratio of 0.710247 ± 0.000002 2σ SE and 0.000025 2σ SD

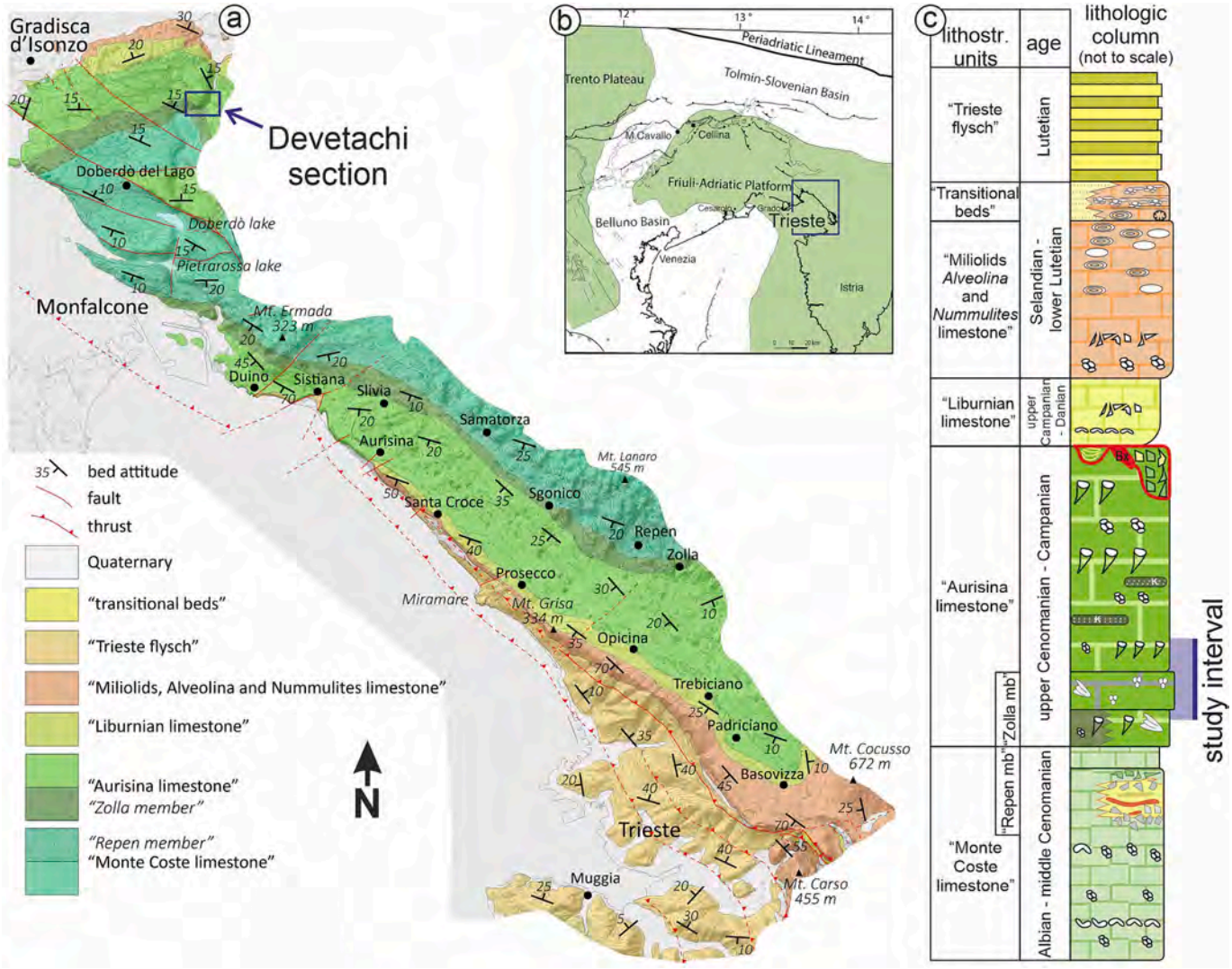

Fig. 1. Location and lithology of the studied area (modified from Consorti et al., 2021). 1a. Geological map of the Italian Karst (simplified from Jurkovšek et al., 2016). 1b. Cretaceous palaeogeographic map (after Picotti et al., 2019). 1c. Lithostratigraphic units and lithological columns of the studied area.

(n = 185) for NIST NBS 987, and a $^{87}Sr/^{86}Sr$ ratio of 0.709168 ± 0.000003 2σ SE and 0.000041 2σ SD (n = 150) for USGS EN-1. Errors of $^{87}Sr/^{86}Sr$ ratios are reported in 2σ SE. The $^{87}Sr/^{86}Sr$ ratios of the samples were adjusted to a value of 0.709175 for the USGS EN-1 standard, to be consistent with the normalization used in the compilation of the 'look-up' table of McArthur and Horwath (2020, version 6) for age calculation. Details of the procedures for deriving numerical ages from Sr-isotope data are available in the Supplementary material following the approach of Frijia et al. (2015).

To carefully assess the preservation of the original shell microstructure, the elemental composition of the shells (Mg, Sr, Mn, and Fe) was employed as further diagenetic criteria to complement optical microscopy observations. For measuring the concentrations of Mg, Sr, Fe, and Mn, about 1.5 mg of the produced sample powder was dissolved in 1 ml 3 M HNO3. Subsequently, 2 ml of H_2O was added, and the samples were left to react for 24 h before being analyzed. The elemental concentrations (Mg, Sr, Fe, Mn) were measured with an Inductively Coupled Plasma Optical Emission Spectrometer (ICP-OES, Thermo Fisher Scientific iCAP 6500 DUO). The standards BCS-CRM512 (dolomite; Bureau of Analyzed Samples Ltd) and BCS-CRM513 (limestone) were regularly analyzed with a long-term 1σ-reproducibility for BCS-CRM512 (n = 178; 2019–2023) of 0.3 Ca (wt%),0.2 Mg (wt%), 0.002 Sr (wt%), 0.001 Fe (wt%), 0.0001 Mn (wt%) and for BCS-CRM513 (n = 175; 2019–2023) of 0.5 Ca (wt%), 0.002 Mg (wt%), 0.0003 Sr (wt%), 0.001 Fe (wt%), 0.0002 Mn (wt%). Strontium isotope and elemental analyses were performed at the Institute for Geology, Mineralogy, and Geophysics of Ruhr University (Bochum, Germany).

4. Results

4.1. Facies analyses

Based on semi-quantitative petrographic analyses of thin sections, seven main lithofacies (LFs) were identified and interpreted in terms of depositional environment considering the texture, components, and sedimentary structures, and following the criteria proposed by Flügel (2004). All the identified LFs can be ascribed to an inner platform/shelf setting. Table 1 and Figs. 2 and 3 highlight the main characteristics of the identified LFs (textures, components, and inferred depositional environments) whereas detailed LF descriptions are reported in the Supplementary information.

Based on the sedimentological and lithological characteristics, the section was subdivided into 6 intervals (Fig. 2).

Interval 1 (0–20 m): Is dominated by lagoonal deposits of LF4 in the first 5–7 m, followed by bindstones of LF1 and peloidal packstone/grainstone of LF3, which become increasingly abundant upwards,

Table 1
Main sedimentological features of the seven lithofacies identified in Devetachi section. The relative abundance of the different componets (skeletal and non-skeletal grains) is expressed as: (a) abundant, (s) subordinated, (r) rare.

Lithofacies	Components	Sedimentary and diagenetic features	Depositional settings
LF1 Laminated wackestone to bindstone	micritic intraclasts (a), micropeloids (a), bivalve/rudists (s), ostracods (s), small benthic foraminifera (s), gastropods (s), calcisphaeres(r)	faint crinkle lamination, clotted micropeloidal fabric and occasional calcimicrobial texture, bivalve fragments; slightly argillaceous	restricted dysoxic intertidal to shallow subtidal
LF2 Micropeloidal mudstone-wackestone to packstone	micropeloids (a), ostracods (s), *Thaumatoporella* (s), benthic foraminifera (s), nubeculatids (s), cyanobacteria filaments (r), Dasycladaceans (r), bivalve (r)	fenestrae (a), vugs (a), bivalve fragments, small benthic foraminifera	supratidal-intertidal
LF3 Peloidal packstone to grainstone	peloids (a), bivalve (r), benthic foraminifera (r), ostracods (r), *Thaumatoporella* (r), micritic intraclasts (r)	vugs (r), bivalve fragments, small benthic foraminifera	restricted shallow lagoon
LF4 Foraminifera wackestone-packstone	benthic foraminifera (a), peloids (a-s), *Thaumatoporella* (s), bivalve (s)	large and small benthic foraminifera, large bivalve fragments mainly composed by rudists	shallow lagoon with water circulation
LF5 Gastropod packstone to floatstone	large gastropods (a), green algae (s), peloids (s), rudists (r)	large gastropods (0.5 to a few cm) mainly whole shells, rudist fragments	shallow to open lagoon
LF6 Microbioclastic-bivalve wackestone-packstone with calcispheres	microbioclastic debris (a), bivalves (a), calcisphaere (s), gastropods (r), coral fragments (r)	thin bivalve fragments, often articulated, small gastropods	open lagoon with low to moderate water energy
LF7 Bivalve packstone-rudstone	bivalves (a)	rudists and *Chondrodonta* bivalves	open lagoon with moderate to high water energy
LF7a Bivalve packstone	bivalve fragments (a), echinoderms (s)	undetermined highly fragmented bivalves, echinoderm fragments	
LF7b Rudist packstone-rudstone	rudists (a), *Chondrodonta* (s)	thin elongated rudist fragments, *Chondrodonta* fragments	
LF7c Rudist packstone to floatstone/ rudstone	rudists (a), peloids (s), benthic foraminifera (r)	large whole and fragmented rudist shells mostly toppled but occasionally found in life position, small benthic foraminifera	
LF7d *Chondrodonta* floatstone-rudstone	*Chondrodonta* (a), rudist (s)	*Chondrodonta* shells mostly articulated and not intensily fragmented, rudist shell fragments	

intercalated to LF4, for the next 10 m. Two levels of LF1 with sporadic calcispheres are found from meters 10 to 15. The last 5 m of this interval represent a shift to slightly deeper conditions with the occurrence of LF7a-d and LF4. A few levels of microbioclastic-bivalve packstone with few calcispheres of LF6 are found from meters 15 to 19.

Interval 2 (20–40 m): Is dominated by medium (40–50 cm) to thick strata (up to 80 cm) of LF7. *Chondrodonta* (LF7d) are abundant in the lower and upper part of the interval while highly fragmented rudist packstone-rudstones (LF7b) with very poorly preserved foraminifera dominate the middle part.

Interval 3 (40–60 m): It consists of an alternation of very shallow subtidal LF1 and LF2 with the sporadic occurrence of large gastropod-dominated LF 5 at meters 46 and 55, forming beds of a maximum of 30 cm. Upwards, the interval is capped by 1.5 m of thin beds of rudist LF7c.

Interval 4 (60–90 m): Is characterized by the shallowest depositional conditions of the entire section. It is dominated by LF2 intercalated with LF3. Fenestrae, cemented vugs, and evidence of at least two emersion surfaces (at 66 and 72 m) are found in thin sections and the outcrop. Bioturbation with *Thalassinoides*-like ichnofacies is found in the middle of this interval.

Interval 5 (90–117 m): Is composed of two 10–13 m thick cycles whose base is composed of medium-thickness rudist beds of LF7c passing upwards to LF1-LF2 and LF3 with evidence of ephemeral emergence represented by micro dissolutions features and cemented vugs. The occurrence of closely spaced thick-bedded rudist strata of LF7c marks the top of this interval.

Interval 6 (115–145 m): Is dominated by thick (up to 1 m) rudist-rich beds of LF7c. Rudist shells are mainly fragmented and of variable size (up to 4–7 cm). Rare complete shells were observed in the outcrop. Rudists are chaotically distributed within the beds, even in rare cases of thin intervals with shells oriented parallel to the stratification. Occasionally, on the top of LF7c, LF1 occurs.

4.2. Biostratigraphy

The biostratigraphic framework was determined by analyzing the vertical distribution of the benthic foraminifera identified in thin sections. The inferred age refers to published records of coeval peri-Mediterranean carbonate platforms (Chiocchini et al., 2012; Schroeder and Neumann, 1985; Velić, 2007) where the assemblage zones, although reliable in terms of relative occurrences, are not definitively anchored to the chronostratigraphic scale. The stratigraphic range of some of the identified taxa is further constrained by correlating their distribution in the section with published records calibrated with chemostratigraphic tools (Arriaga et al., 2016; Frijia et al., 2015). Moreover, this study highlights new records of benthic foraminifera that have not been reported previously from this stratigraphic position. The most relevant identified taxa are illustrated in Fig. 4.

The basal 20 m of the section (interval 1) contains *Pastrikella balcanica* (Cherchi, Radoičić & Schroeder) *Rotorbinella mesogeensis* (Tronchetti), *Chrysalidina gradata* d'Orbigny, *Pseudorhapydionina dubia* (De Castro) and *Vidalina radoicicae* Cherchi & Schroeder, that can be considered as a reliable proxy of the upper Cenomanian substage (Frijia et al., 2015; Schroeder and Neumann, 1985). Through this stratigraphic interval, accompanying fauna is represented by *Nummoloculina* sp., *Nezzazata isabellae* Arnaud-Vanneau & Sliter, *Nezzazata conica* (Smout), and *Dicyclina* cf. *schlumbergeri* Munier-Chalmas. This interval is followed by about 25 m (interval 2) barren of foraminifera, where just sporadically some small miliolids and discorbidae were observed, whereas, towards the upper part, the green algae *Heteroporella* cf. *lepina* Praturlon occurs.

A new foraminiferal assemblage makes its first appearance at meter 40 (interval 3) where none of the species identified through the first 20 m interval have been found. It is composed, up to meter 90, of *Moncharmontia apenninica* (De Castro), *Braciana* sp. and *Rotalispira* sp.,

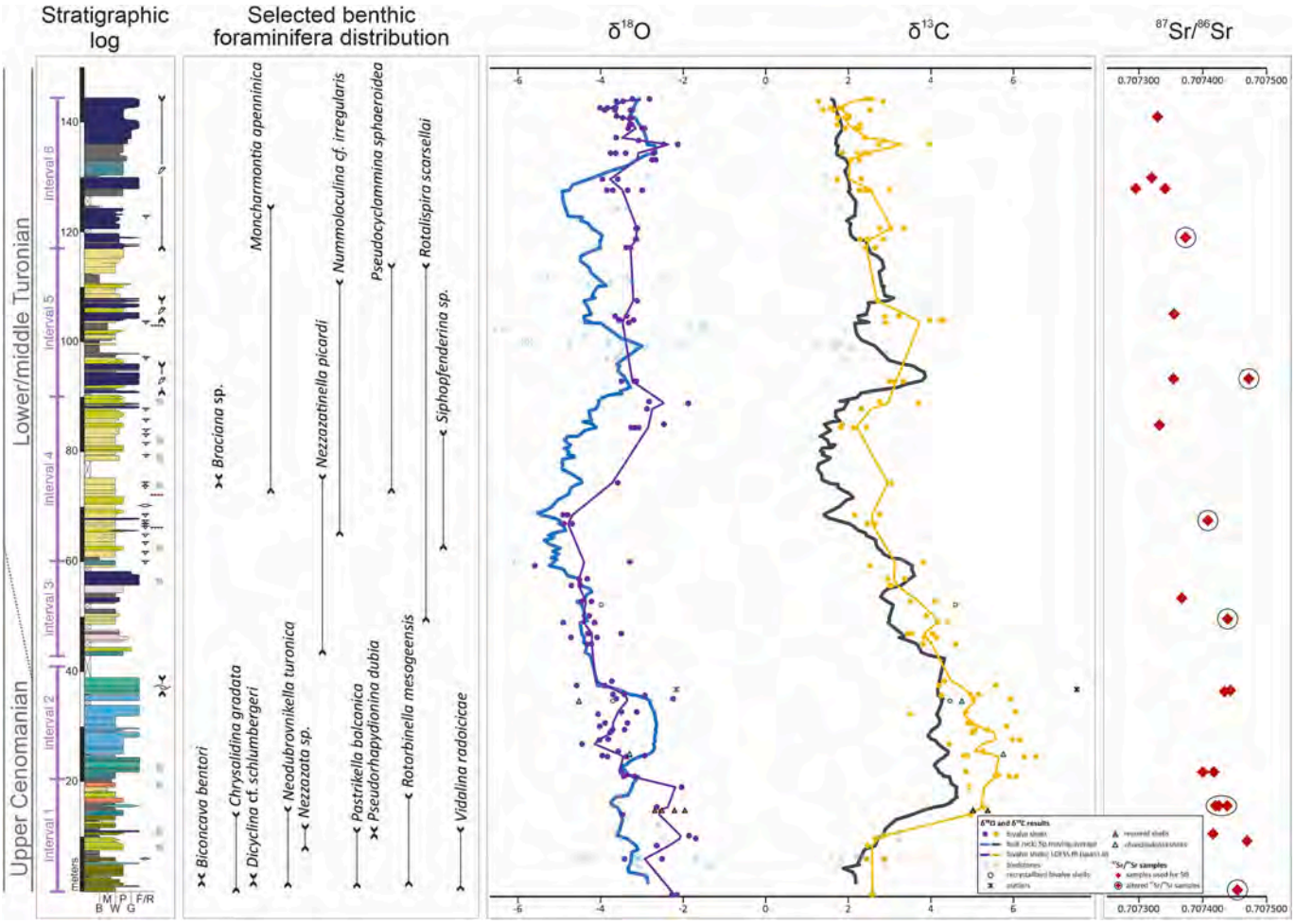

Fig. 2. Lithological-sedimentological log, biostratigraphy, chronostratigraphy, and isotope stratigraphy of Devetachi section. Chronostratigraphic calibration is constrained by biostratigraphy. B, bindstone; M, mudstone; W, wackestone; P, packstone; G, grainstone; F/R, floatsone/rudstone. The dotted diagonal line represents the Cenomanian-Turonian boundary interval as defined by biostratigraphy, for the LFs definition see text and Supplementary information. Bulk rock $\delta^{18}O$ and $\delta^{13}C$ results are averaged where more samples from one stratigraphic level were analyzed and the resulting curves are smoothed (5 points moving average). The radiolitid, requinid, and *chondrodonta* shell $\delta^{18}O$ and $\delta^{13}C$ curves are smoothed using the LOESS fit (span 1.0). Values corresponding to LF1 are reported (crosses) but excluded from the stable isotope curves (see text for details). Shell samples with evidence of recrystallization were also excluded from the curves. Results of Sr-isotope analyses of all individual measured samples are reported. Altered shells are marked with a black circle.

Rotorbinella sp., *Nezzazatinella* sp., resembling *N. aegyptiaca* (Said & Kenawi), *Nezzazatinella picardi* (Henson), *Siphopfenderina* sp., *Pseudocyclammina sphaeroidea* Gendrot, *Spiroplectammina multicamerata* Said & Kenawy, *Valvulina* sp., and *Nummoloculina* cf. *irregularis* (d'Orbigny), along with miliolidae and discorbidae. Based on correlations with Sr-isotope stratigraphy (SIS) data from the Apennine Carbonate Platform (ACP) of Arriaga et al. (2016) and Frijia et al. (2015), and the occurrence of the index assemblage *Nezzazatinella*, *M. apenninica,* and *P. sphaeroidea*, it is possible to assign this stratigraphic interval to the lower-middle Turonian.

From meter 90 (interval 5) to the top of the section, the foraminiferal assemblage is characterized by the co-occurrence of *Nezzazatinella picardi*, *Pseudocyclammina sphaeroidea*, *Rotorbinella* sp. (very close to *Eponides hemisphaericus* in Chiocchini et al., 2012), *Rotalispira scarsellai* (Torre), *Moncharmontia apenninica* and *Nummoloculina* cf. *irregularis*, along with miliolidae and discorbidae. On this basis and considering both SIS and classical biostratigraphy (Arriaga et al., 2016; Chiocchini et al., 2012; Frijia et al., 2015) it was possible to place the upper part of the studied section in the middle Turonian. The CTB could be placed within the fossil-free interval 2, whereas community recuperation related to the post-extinction aftermath starts from interval 3.

4.3. Carbon and Oxygen isotopes

Closely spaced sampling permitted the construction of a high-resolution $\delta^{13}C$ and $\delta^{18}O$ record both from bulk-rock and bivalve shell samples (Fig. 2). The bulk-rock curves are represented as five-point moving averages to remove "noise" and small-scale perturbations of raw-data profiles.

In both the $\delta^{13}C$ and $\delta^{18}O$ records, marked low-value peaks occur, corresponding to vuggy/ fenestral-rich facies or close to emersion surfaces (Fig. 2). These values were not considered in the calculation of the moving averages. Also, the laminated carbonates of LF1 were not considered for the moving average curves following the results in Frijia et al. (2019, see discussion below). The $\delta^{13}C$ averaged values of bulk rock material, range from a minimum of 2.7 ‰ to a maximum of 5.1 ‰, whereas the $\delta^{18}O$ values range from a minimum of −6.1 ‰ to a maximum of −1.6 ‰. The shell values were obtained mainly from well-preserved fragments of radiolitid rudists, with one level containing requinid rudists, and two levels of *Chondrodonta* shell fragments. The $\delta^{13}C$ shell values range from 1.3 ‰ to 6.6 ‰, and in $\delta^{18}O$ from −5.6 ‰ to a maximum of −1.7 ‰. The resulting secular $\delta^{13}C$ and $\delta^{18}O$ trends of bulk rock and shell material are closely similar, with shell fragments generally yielding slightly higher $\delta^{13}C$ and $\delta^{18}O$ values.

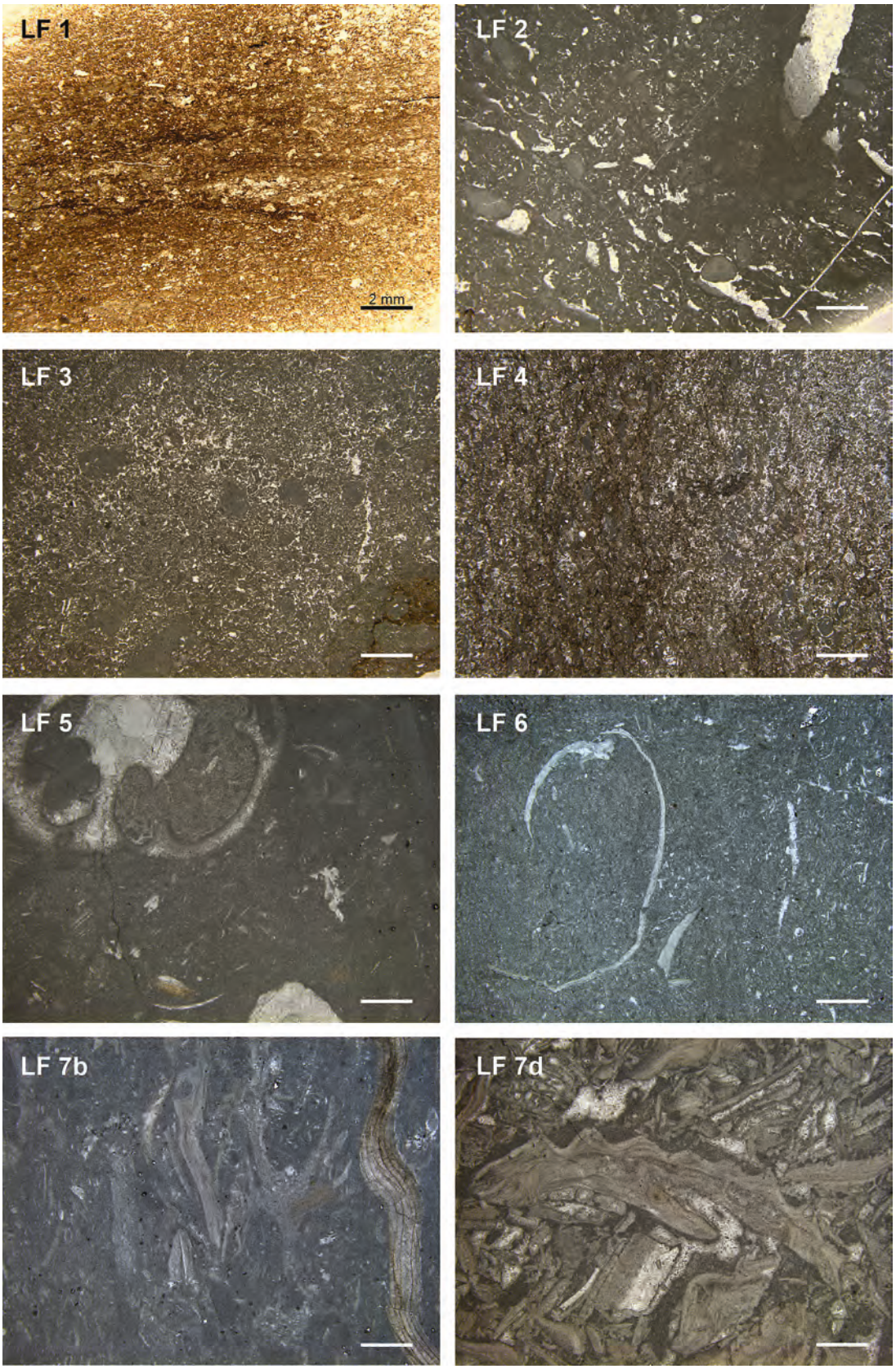

Fig. 3. Some representative photomicrographs of the facies identified in the studied sections (LF 7a and 7d are not pictured). LF1 Laminated micropeloidal wackestone to bindstone; LF2 Mudstone-wackestone to packstone often with fenestrae and/or vugs; LF3 Peloidal packstone to grainstone; LF4 Foraminifera wackestone-packstone with peloids: LF5 Gastropod packstone to floatstone; LF6 Microbioclastic-bivalve wackestone-packstone with calcispheres; LF7b Rudist packstone-rudstone with highly fragmented, thin-elongated fragments of radiolitid rudists and subordinated *Chondrodonta* shell fragments: LF7d *Chondrodonta* floatstone-rudstone. Scale bar is 2 mm for all the photographs.

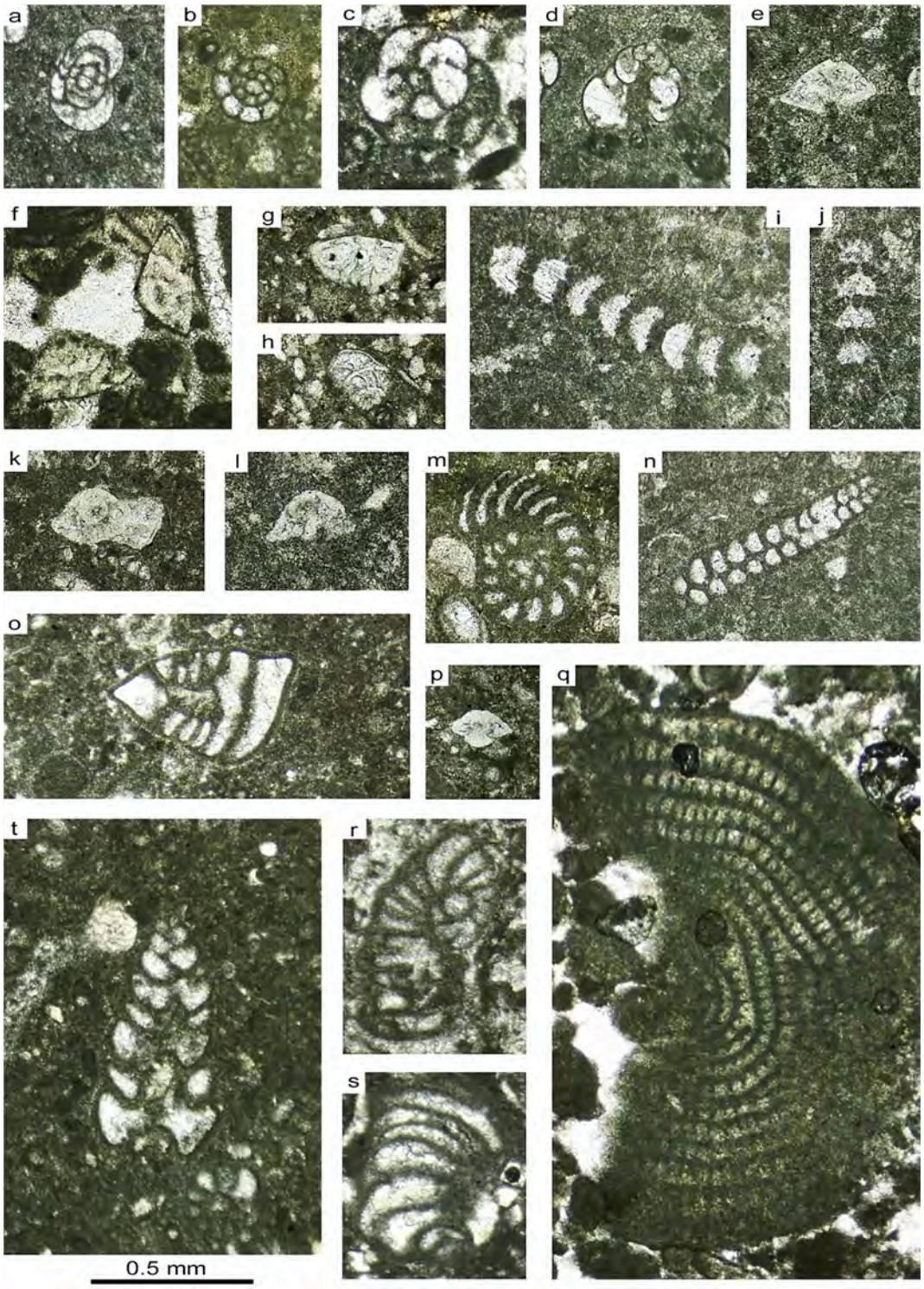

Fig. 4. Selected foraminifera specimens from Devetachi section. a, b) *Moncharmontia apenninica.* c, d) *Siphopfenderina* sp. e, k) *Rotalispira* sp. f) *Rotorbinella* sp. g, h) *Rotalispira scarsellai.* i, j) *Braciana* sp. l) *Rotorbinella* sp. (=*Eponides hemisphaericus* in Chiocchini et al., 2012). m) *Pseudocyclammina sphaeroidea.* n) *Spiroplectammina multicamerata.* o) *Nezzazatinella picardi.* p) *Rotorbinella mesogeensis.* q) *Pastrikella balcanica.* r, s,) *Neodubrovnikella turonica.* t) *Valvulina* sp. Scale equals 0.5 mm for all the specimens.

At the base of the section (intervals 1 and 2), the smoothed bulk rock $\delta^{13}C$ isotope curve (Fig. 2) shows a pronounced shift to high values (from meter 13) culminating in a maximum of 4.6 ‰ above meter 20. For the following 20 m, the $\delta^{13}C$ curve shows the highest values of the whole section, around 4.2 ‰. From meter 40 to 90 (intervals 3 and 4), the carbon isotope values present a regular decrease, with superimposed minor fluctuations towards higher values (slightly <1 ‰), reaching a minimum value of 0.8 ‰ just below the base of interval 5. Continuing upwards, in the first meters of interval 5, the $\delta^{13}C$ values increase rapidly to a peak of 4 ‰ at 95 m. After this point, the $\delta^{13}C$ bulk curve shows a regular lowering of the values until the top of the section which have the lowest value of 1.5 ‰.

The $\delta^{18}O$ profile of both bulk-rock and shells shows a general decreasing trend from the base of the section where values around −2.5 ‰ are found, to the lowest values of the whole section between 60 and 70 m (around −5.5 ‰ in interval 4). This general trend is interrupted by a fluctuation to higher $\delta^{18}O$ values in interval 2 which is evident in the bulk rock curve but less pronounced in the shells isotopic record. A gradual increase in $\delta^{18}O$ values follows until meter 100 before a slightly lowering trend occurs from meter 110 to 130. From meter 130 to the top

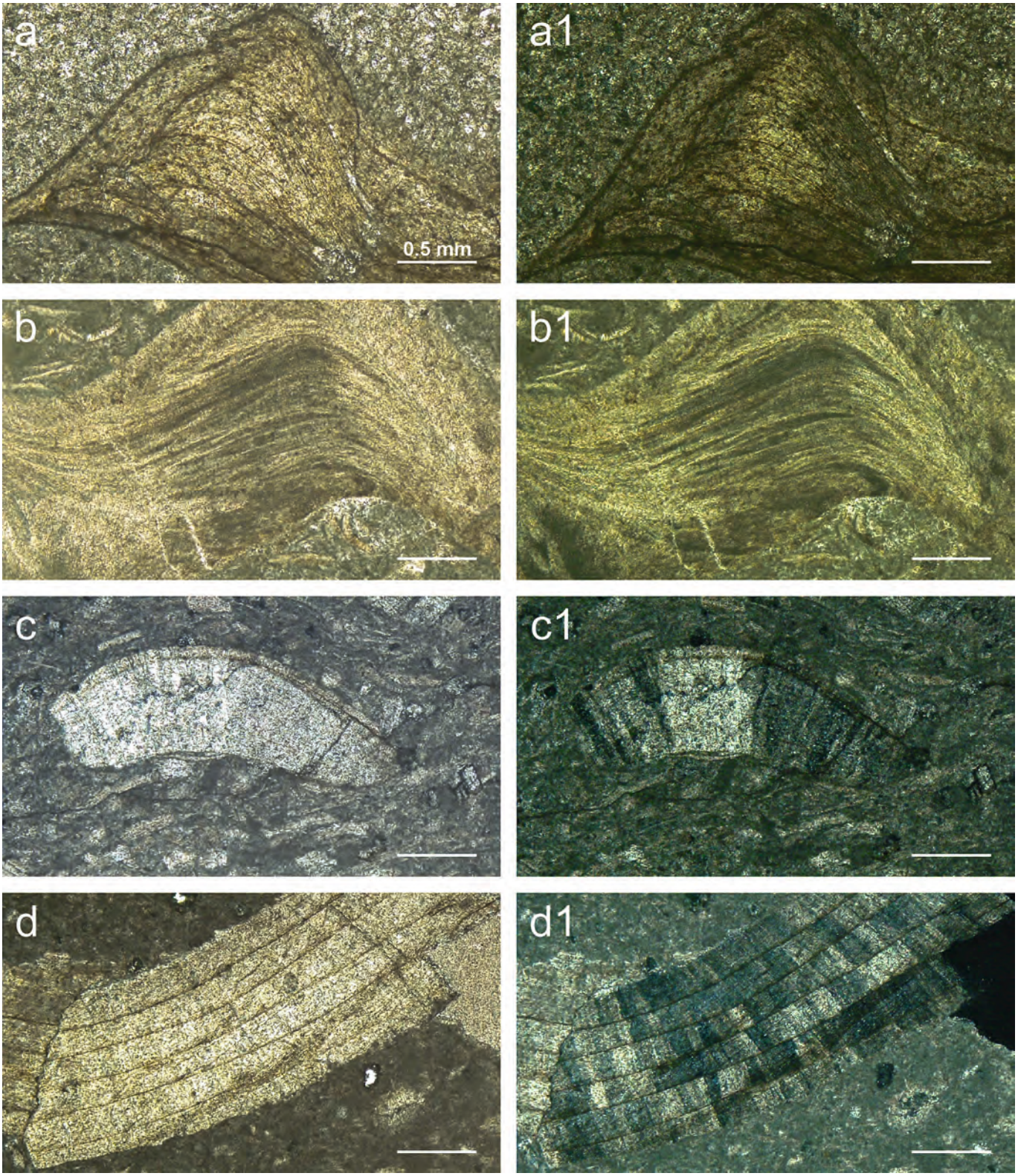

Fig. 5. Thin sections of rudist shells and *Chondrodonta*. A-B well-preserved cross-foliated microstructure of chondrodonta shell (A1-B1 crossed nicols); C—D compact portion of the outer shell layer of two different radiolitid shells. Fig. C1 (crossed nicols) shows slight recrystallization of the prismatic microstructure, fig. D1 shows well-preserved prismatic structure and growth lines. Scale bars equal 0.5 mm.

of the section, the values rise to around −3 ‰ and remain constant.

4.4. Sr-isotope stratigraphy (SIS)

Several studies have shown that the low-Mg calcite rudist shells are among the material most suitable for SIS (Frijia et al., 2015 and references therein). The analyzed rudist samples show excellent preservation of the original prismatic microstructure (Fig. 5). To obtain further insight into the diagenetic processes, concentrations of major and trace elements (Sr, Mg, Fe, and Mn) were measured (Fig. 6). A threshold for Sr content of 800 ppm for well-preserved rudist shells (Frijia et al., 2015; Huck and Heimhofer, 2015; Steuber, 1999, 2003; Steuber et al., 2005b) was used to assess sample preservation. Four samples having Sr content below 800 ppm were considered diagenetically altered and thus were excluded from further $^{87}Sr/^{86}Sr$-based age calculations. Considering the very consistent and low concentration of Mn (>8 ppm) and Fe (>25 ppm) in all analyzed samples (well below the diagenetic threshold usually reported for these elements in biotic carbonates; see Frijia et al., 2015 and reference therein), one sample with Fe content of ~60 ppm was also considered to be diagenetically-altered and not used in further interpretations despite its relatively high Sr content.

Furthermore, 3 samples were excluded from the SIS database as their isotopic $^{87}Sr/^{86}Sr$ values are more radiogenic than samples from the nearby interval, considering that diagenesis usually raises $^{87}Sr/^{86}Sr$ signal (Boix et al., 2011; McArthur, 1994, p. 19). Among the samples selected for SIS, the highest Sr isotope values are found in the lower part of the section (intervals 1 and 2; upper Cenomanian) where they range from 0.707416 to 0.707417. In the overlying interval, the samples show a regular decrease of the Sr-isotopic values until a minimum of 0.707319 is reached (interval 6). This trend mirrors the decrease in Sr-isotope values which characterizes the late Cenomanian-late Turonian interval of the global marine Sr-isotope secular curve (McArthur and Horwath, 2020). Interestingly, the Sr-isotope values from the lower part of Devetachi section (intervals 1–2) are comparable within error with those found in the upper Cenomanian shallow-water carbonates of the ACP (; Frijia and Parente, 2008a). As highlighted by these authors, the discrepancy between the high-resolution Sr-isotopic data measured across the late Cenomanian in the ACP and the modelled Sr-isotopes marine reference curve hampers the use of SIS for this stratigraphic interval (Frijia and Parente, 2008a). Therefore, it was not possible to interpret the $^{87}Sr/^{86}Sr$ values from the lower part of Devetachi section in terms of numerical ages. The calculated SIS ages from the selected post-Cenomanian beds are reported in Table 2 and discussed in the following paragraphs together with the $\delta^{13}C$-isotope stratigraphy.

5. Discussion

5.1. Reliability of $\delta^{13}C$ and $\delta^{18}O$ geochemistry

The C and O isotope composition of shallow-water carbonates is known to be potentially affected by *syn-* and post-depositional diagenetic alteration (Marshall, 1992), biological fractionation, and local environmental processes which can cause the isotopic signal to deviate from the global open ocean value (Del Viscio et al., 2022 and references therein). Positive covariance between $\delta^{13}C$ and $\delta^{18}O$ bulk rock values is characteristic though not diagnostic of diagenetic alteration due to meteoric water influx in the mixing zone (Allan and Matthews, 1982) as well as decreasing alteration in the freshwater phreatic zone (Swart and Oehlert, 2018). Although the lack of covariance between $\delta^{13}C$ and $\delta^{18}O$ alone has been proposed as indicative of the unaltered nature of the isotopic signal (Grotzinger et al., 2011), recent studies point out that changes in the sediment source through time can also produce paired shifts in $\delta^{13}C$ and $\delta^{18}O$ values (Oehlert and Swart, 2019; Swart and Oehlert, 2018).

In Devetachi section, cross-plots of $\delta^{13}C$ and $\delta^{18}O$ values for single facies show that they plot within the field of Cretaceous well-preserved low-latitude biotic calcite (after Veizer and Prokoph, 2015; Fig. 6e), apart from the LFs 6, 7b, and 7d that show higher $\delta^{13}C$ values. These LFs are composed of abundant bivalve shell material (mainly rudists) and, possibly, their high values correspond to the wide range of variability of C-isotopes in mollusk shells, due to their metabolic activity (Walliser and Schöne, 2020) and their response to perturbed C-cycle associated with Oceanic Anoxic Event 2 (see next paragraph).

The lowest $\delta^{13}C$ and $\delta^{18}O$ values (Fig. 6e) are found in LF1 and LF2. These laminated carbonates of LF1 are of probable bacterial origin/influence and likely do not preserve the original isotopic signature of the seawater due to their metabolic processes as found by Frijia et al., 2019 in coeval facies of the ACP.

LF2 contains some spar-filled fenestrae and vugs, indicating deposition in a supra-intertidal environment that was possibly subject to short-lasting subaerial exposure episodes. Nevertheless, $\delta^{13}C$ and $\delta^{18}O$ values of this LF2, fall well within the field of well-preserved biotic calcite of shallow marine tropical-subtropical carbonates (Veizer and Prokoph, 2015). Finally, the inverted "J" stable isotope pattern, typical of carbonates affected by meteoric diagenesis (Allan and Matthews, 1982; Lohmann, 1988) is not present in the analyzed samples dataset, indicating that the isotope patterns did not suffer from significant meteoric alteration.

The reliability of the bulk rock isotopic data can be cross-checked by comparison to the shells isotopic composition. Well-preserved rudists are considered to record the $\delta^{13}C$ and $\delta^{18}O$ of the water they grew in. There is a consensus that fractionation for $\delta^{18}O$ occurs in equilibrium with the fluid, whereas a more variable $\delta^{13}C$ signal can be found, due to metabolic processes (Steuber, 1999; Walliser and Schöne, 2020).

We consider the radiolitid shells isotopic record presented in this study to reflect the original isotopic composition of the seawater, given that: 1) radiolitids proved to precipitate their shells in equilibrium with sea-water $\delta^{13}C$ and $\delta^{18}O$ (e.g., Schmitt et al., 2022). 2) The isotopic values of the radiolitid shells in this study are comparable with the data of Frijia (2006), Frijia et al. (2015) and (Frijia et al. (2019)) for the Late Cenomanian-Campanian interval of the ACP (Fig. 6f) and with the $\delta^{18}O$ values of well-preserved Late Cretaceous rudists of Steuber et al. (2005b). 3) The analyzed radiolitids show very good preservation of their prismatic outer shell layer (Fig. 5). 4) The C and O isotope composition of the samples considered as well preserved, based on elemental analyses, is within the range of that observed in radiolitid fragments which preservation was assessed only by petrographic analyses of the microstructures. Only a few samples appeared slightly recrystallized under optical microscopy but their $\delta^{13}C$ and $\delta^{18}O$ values do not differ from that of preserved samples (Fig. 6f).

The close resemblance of bulk rock and the shell $\delta^{13}C$ and $\delta^{18}O$ profiles suggests good preservation of the original marine isotopic signal in the bulk rock material. Interestingly, this finding was unanticipated given that the oxygen isotopic records in shallow marine carbonates are easily altered by diagenetic processes (Marshall, 1992).

5.2. Chemostratigraphy ($\delta^{13}C$, $^{87}Sr/^{86}Sr$)

A correlation among the major features of the carbon-isotope profile of the bulk curve from Devetachi section, the Late Cretaceous marine $\delta^{13}C$ reference curve (Cramer and Jarvis, 2020), and the high-resolution Turonian pelagic carbon-isotope curve from the Bohemian Cretaceous Basin (Jarvis et al., 2015) is presented in Fig. 7.

The reference curve of Cramer and Jarvis (2020) shows a very prominent positive carbon-isotope excursion (CIE) of about 3 ‰ at the Cenomanian-Turonian boundary interval (Fig. 7), corresponding to the Oceanic Anoxic Event 2 (OAE-2, Paul et al., 1999; Tsikos et al., 2004). The following positive CIEs are short-lasting and smaller in amplitude, occurring during the early (Holywell and Lulworth events) and middle Turonian (Round Down and Low-Woollgari events). Matching of Devetachi carbon-isotope curve with the reference/pelagic records was constrained by cross-correlating the CIEs and by independent tie-points,

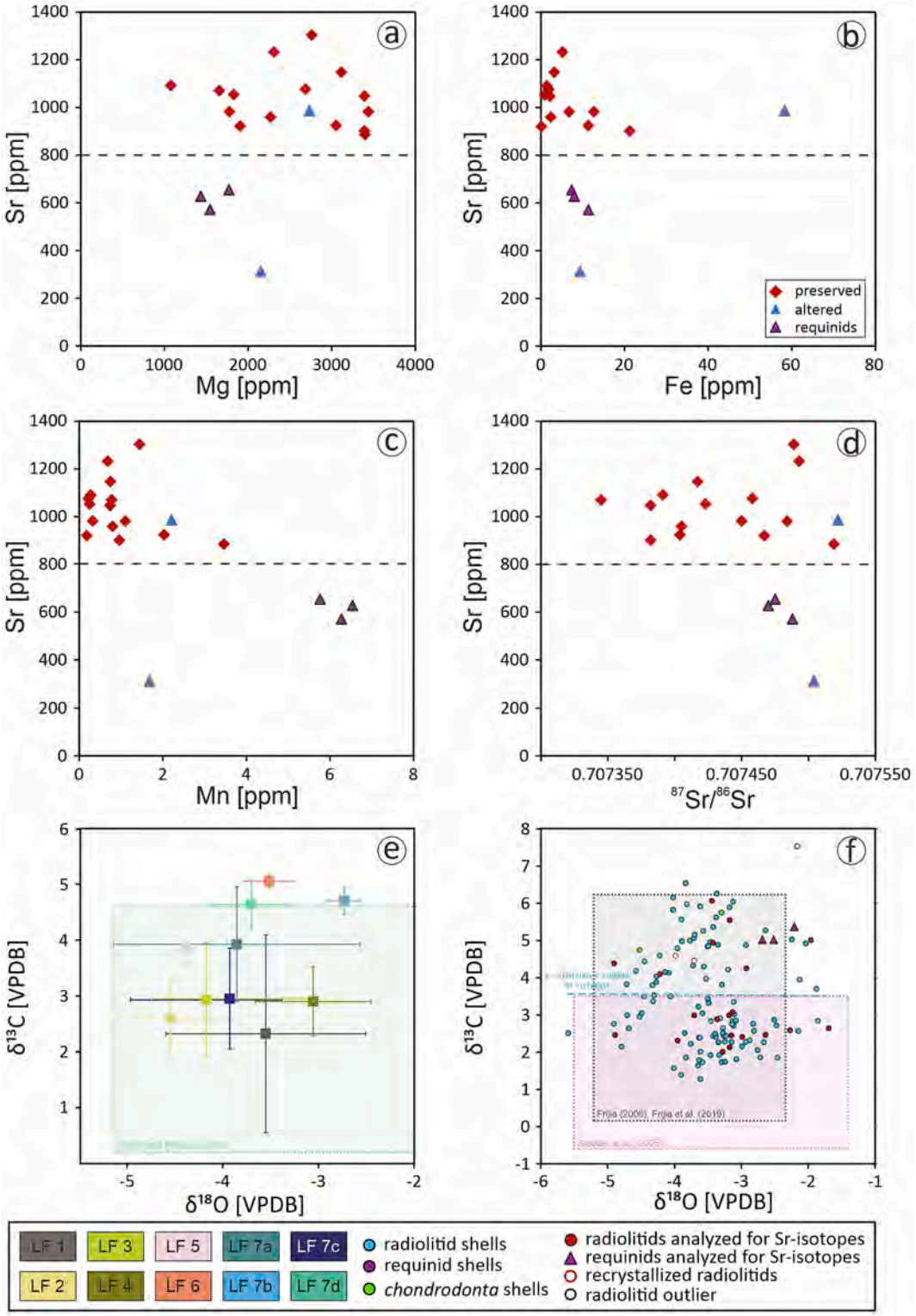

Fig. 6. Cross-plots of elemental and stable isotope analyses. a-d. Mg, Fe, and Mn. vs. Sr concentrations and Sr vs. $^{87}Sr/^{86}Sr$. The dashed horizontal line indicates the threshold Sr concentration (800 ppm) used in this study after Steuber et al. (2005b) and Frijia et al. (2015). Above this value, it is assumed that the original marine Sr-isotopic ratio has been retained (see text for further details). Note that most of the rudist samples analyzed in this study have very low Fe and Mn concentrations except for one sample with a Fe concentration of 58 ppm, which was excluded from Sr-isotope stratigraphy (see text for details). Samples stratigraphically belonging to CTBE are marked (and were not considered for SIS; see text for details). e. Average $\delta^{18}O$ and $\delta^{13}C$ of individual lithofacies (error bars indicate the standard deviation of the averages). The rectangle represents the well-preserved biotic calcite of shallow marine tropical-subtropical carbonates (after Veizer and Prokoph, 2015; in green). f. Cross-plot of $\delta^{18}O$ vs. $\delta^{13}C$ values. Individual bulk rock (crosses) and bulk shell (points) values show no covariance between $\delta^{18}O$ and $\delta^{13}C$. Values corresponding to LF1 are reported (in grey) but are not included in the reported equations, as well as shell samples showing evidence of recrystallization. The rectangles represent the range of well-preserved Late Cretaceous rudists (Steuber et al., 2005a,b; in pink), and well-preserved radiolitids (Frijia, 2006; Frijia et al., 2019 in black). (For interpretation of the references to colour in this figure legend, the reader is referred to the web version of this article.)

Table 2
Sr-isotope stratigraphy, elemental concentrations and $\delta^{18}O$-$\delta^{13}C$ isotopic composition of rudist shells from Devetachi section.

Samples	Meters from the base	$^{87}Sr/^{86}Sr$ measured	± 2 s.e.n	87Sr/86Sr corrected	87Sr/86Sr mean	± 2 s.e. mean for age calculation	Min. [Ma]	Age Preferred [Ma]	Max. [Ma]	Mg [ppm]	Sr [ppm]	Fe [ppm]	Mn [ppm]	$\delta^{18}O$ [‰ VPDB]	$\delta^{13}C$ [‰ VPDB]
DSS0.3-B	*0.3*	*0.707455*	*0.000005*	*0.707454*						2152	313	9	2	−2.27	2.59
DSS9.2-A	*9.2*	*0.707496*	*0.000006*	*0.707469*						3399	886	n.d.	3	−2.64	2.47
DSS10.5-A	*10.5*[*]	*0.707423*	*0.000005*	0.707416						n.d.	n.d.	n.d.	n.d.	−1.69	2.64
CAP4–3-A	*15.6*[*]	*0.707439*	*0.000005*	*0.707438*						1546	572	11	6	−2.52	5.02
CAP5–2-A	*15.6*[*]	*0.707426*	*0.000005*	*0.707425*						1771	655	7	6	−2.68	5.02
CAP5–2-C	*15.6*[*]	*0.707427*	*0.000005*	*0.707420*						1433	628	8	7	−2.21	5.38
DSS21.75-A	*21.75*[*]	*0.707401*	*0.000005*	0.707400						1775	983	7	0	−3.17	5.55
DSS21.75-C	*21.75*[*]	*0.707418*	*0.000005*	0.707417						1905	921	0	0	−3.44	6.07
SD0.4-A	*36.4*[*]	*0.707435*	*0.000007*	*0.707434*						3437	982	13	1	−2.92	4.25
SD0.6-B	*36.6*[*]	*0.707444*	*0.000007*	*0.707443*						2310	1233	5	1	−3.43	4.94
SD13.6-B	*49.6*	*0.707440*	*0.000006*	*0.707439*						2759	1304	n.d.	1	−4.90	4.39
SD17.4-A	*53.4*	*0.707370*	*0.000005*	0.707367	0.707367	0.000018	93.1	**93.8**	94.6	3113	1148	3	1	−4.22	4.10
SD31.5-A	*67.5*	*0.707411*	*0.000005*	*0.707408*						2686	1077	2	0	−4.89	2.46
SD48.9-B	*84.9*	*0.707339*	*0.000005*	0.707332	0.707332	0.000018	91.90	**92.7**	93.5	3391	902	21	1	−3.18	2.13
SD58.3-A-A	*93.3*	*0.707499*	*0.000006*	*0.707472*						2733	987	58	2	−3.18	2.99
SD57.3B-B	*93.3*	*0.707357*	*0.000005*	0.707354						3051	1048	2	1	−3.13	3.08
SD69.1-B	*105.1*	*0.707358*	*0.000005*	0.707355	0.707355	0.000013	92.80	**93.4**	94.0	2267	924	11	2	−3.36	2.89
SD83-A	*119*	*0.707381*	*0.000004*	*0.707373*						1828	960	2	1	−3.15	2.45
SD91.9-A	*127.9*	*0.707353*	*0.000005*	0.707341						1078	1054	1	0	−2.99	2.41
SD91.9-B	*127.9*	*0.707322*	*0.000005*	0.707295						1657	1092	1	0	−3.71	2.99
SD93.9-A	*129.9*	*0.707322*	*0.000004*	0.707320	0.707319	0.000027	na	**92.3**	93.3	1424	1071	2	1	−3.95	2.31
SD105-AA	141	0.707336	0.000005	0.707329	0.707329	0.000018	91.8	**92.6**	93.4	n.d.	n.d.	n.d.	n.d.	−3.28	2.01

Sr-isotope numerical ages from McArthur and Horwath (2020), ("look-up table V6" tied to GTS 2020 from Gradstein et al., 2020).
See text for details on the calculation of numerical ages and on the estimates of the precision.
In Italics samples which have been considered altered (see text for details).
[*] It refers to samples within the OAE-2 for which no age calculation has been made (see text for details).

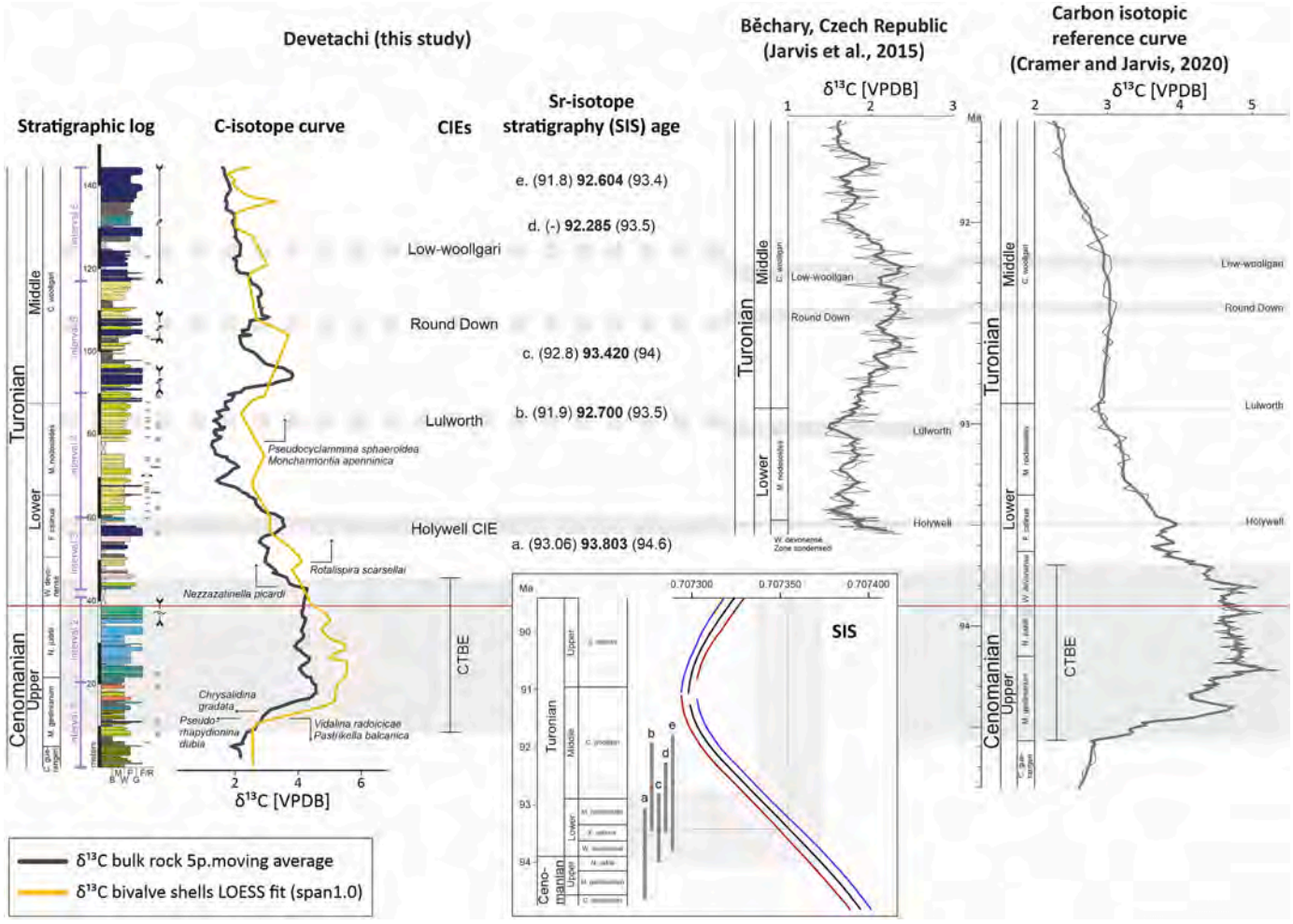

Fig. 7. C and Sr-isotope stratigraphy (SIS) of Devetachi section. C-isotope correlation of the studied section from the Friuli Carbonate Platform with the Late Cretaceous C-isotope reference curve of the English Chalk (Cramer and Jarvis, 2020) and the Turonian carbon-isotope profile of the Bohemian Cretaceous Basin (Jarvis et al., 2015). Black bold numbers indicate the preferred SIS age, whereas the numbers in brackets refer to the upper and lower age limits (see supplementary material for details). Chronostratigraphy of Devetachi section is constrained by chemostratigraphic correlations and biostratigraphy. The inset figure shows the Late Cenomanian-middle Turonian part of the seawater $^{87}Sr/^{86}Sr$ reference curve and the 95% confidence interval (McArthur and Horwath, 2020). Rectangles give the SIS age window obtained combining the uncertainty of the samples with the uncertainty of the curve. In grey, the numerical age calculation of the sample *c* is illustrated as an example.

derived from biostratigraphy and SIS. The very prominent C-isotope positive excursion beginning right below meter 10 in Devetachi section, reaching values of 4 to 6 ‰, can be correlated with the CTB/OAE-2 in the reference curve. Above, the $\delta^{13}C$ curve in Devetachi shows a descending trend similar to the reference curve of Cramer and Jarvis (2020), interrupted by a high-values $\delta^{13}C$ interval, at around 60 m, which is correlated with the Early Turonian Holywell event (Fig. 7). This correlation is strengthened by SIS which gives an age of 93.80 Ma (from a level ~ 12 m below the Holywell event), corresponding to the base of the Turonian (Gradstein et al., 2020). The next match between the $\delta^{13}C$ curve in Devetachi and the reference/pelagic sections is at around meter 80, where the curve reaches its minimum values. This interval can be correlated with the Early/middle Turonian Lulworth event; a correlation reinforced by the SIS ages (Table 2 and Fig. 7) and by biostratigraphy. The local first occurrence (FO) of the benthic foraminifera *M. apenninica* and *P. sphaeroidea* a few meters below supports the position of the Lulworth event in Devetachi section, considering that Frijia et al. (2015) dated the first appearance of these taxa as late Early Turonian. After this isotopic event, the correlation between the shallow and the deep-water C-isotope record is more challenging. Following the Lulworth event in Devetachi, a marked rise of the $\delta^{13}C$ values of around 2 ‰ culminating in a C-isotope peak is observed which appears to have no correlative in the pelagic record. However, in the C-isotope trend from the Bohemian Cretaceous Basin (Fig. 7), a steep rise of around 1.5 ‰ is observed just after the Lulworth event. This culminates in a "saddle/plateau" of $\delta^{13}C$ values where two minor middle Turonian CIEs were identified: the Round down and Low Woollgari events. In Devetachi this $\delta^{13}C$ plateau cannot be easily identified, although the values remain high at around 2–3 ‰ from 95 to 120 m. We have tentatively identified the Round Down event between meters 100 and 105, where the isotopic profile registers a fluctuation towards high values of up to 1 ‰, and the Low-Woollgari event at around 120 m before the lowering of the $\delta^{13}C$ values (Fig. 7). Unfortunately, SIS analysis cannot be used to precisely constrain these two CIEs because the resulting numerical ages are within the error of each other. However, calculated SIS ages between "our" Lulworth and the Low-woollgari events result in a broad interval of 93.4–92.6 Ma, which corresponds to the uppermost lower Turonian and lower middle Turonian (Gradstein et al., 2020). These ages agree with our proposed C-isotope correlation and the biostratigraphy (see section 4.2). Furthermore, the lack of typical benthic foraminifera index taxa such as *Reticulinella kaeveri* and *Scandonea samnitica* identified in coeval platform carbonates (e.g. Southern Apennines, Frijia and Parente, 2008b; Frijia et al., 2015) in the upper middle Turonian interval reinforces our correlation and suggests that the top of Devetachi section is

not younger than the middle Turonian (Fig. 7).

5.3. Oxygen isotopes and $\delta^{18}O$ palaeothermometry

The studies of the Late Cretaceous sea surface temperatures (SSTs) generally rely on $\delta^{18}O$ analyses of planktonic foraminifera (Friedrich et al., 2012; Huber et al., 2018; MacLeod et al., 2013). In contrast, shallow-water carbonates are seldom considered because of an often less continuous sedimentary record and the potential impact of local environmental conditions and diagenesis on the isotopic values (Marshall, 1992; Schmitt et al., 2022). However, the results from Devetachi section suggest that it preserves a fairly complete sedimentary record across the upper Cenomanian-middle Turonian and that the $\delta^{18}O$ signal (in both, the bulk rock and shell fragments) has not been markedly altered.

A comparison of Devetachi $\delta^{18}O$ record with two pelagic sections (Běchary, Czech Republic (Jarvis et al., 2015), and Kent, UK (Jenkyns et al., 1994; Fig. 8), shows remarkable similarities. A warming trend, highlighted by a gradual decrease of the $\delta^{18}O$ values is apparent in both Kent and Devetachi sections from the upper Cenomanian to the Lower Turonian, where the lowest $\delta^{18}O$ values (the warmest interval) occur (Fig. 8, marked in red).

After the minimum $\delta^{18}O$ interval, all three curves show a gradual increase in $\delta^{18}O$ values which testifies to a cooling phase, although interrupted by a few short intervals of lower $\delta^{18}O$ values that could be indicative of warming phases (Fig. 8). A recent exhaustive compilation of Late Cretaceous SSTs using $\delta^{18}O$ in foraminifera and TEX_{86} data indicates the latest Cenomanian-Turonian interval as the warmest time of the whole Cretaceous (O'Brien et al., 2017 and references therein; O'Connor et al., 2019) with the peak warmth in the Early Turonian (Huber et al., 2018; O'Brien et al., 2017). The temperature variations in Devetachi agree with these global temperature reconstructions, suggesting an important impact of global water circulation and heat transfer in shallow marine environments.

Absolute palaeotemperatures in Devetachi section were estimated based on the high-resolution $\delta^{18}O$ record obtained from the shell fragments of radiolitid rudists. Detailed analyses of sclerochornological profiles of these extinct mollusks allowed for the identification and quantification of seasonal temperature changes in shallow water settings of the Cretaceous world (Huck and Heimhofer, 2021; Steuber et al., 2005a). In contrast, the values obtained from rudist fragments analyzed in this study, likely, represent annual/sub annual averages at best and thus do not provide information on seasonal variations. However, they provide, for the first time, high-resolution data on larger-scale temperature evolution in shallow water settings during a critical time interval of the Cretaceous. Rudists-based palaeotemperatures were calculated using the Eq. (1) from Anderson and Arthur (1983):

$$T^{\circ}C = 16.0–4.14*\left(\delta^{18}O_{calcite} - \delta^{18}O_{seawater}\right) + 0.13*\left(\delta^{18}O_{calcite} - \delta^{18}O_{seawater}\right)^2 \quad (1)$$

The challenging aspect when estimating water temperatures based on Eq. (1) is that the $\delta^{18}O_{seawater}$ must be assumed. Most Late Cretaceous palaeoclimatic studies use an average value of −1 ‰VSMOW assuming an ice-free world (e.g., Grossman, 2012; Walliser and Schöne, 2020). This value is often corrected to account for latitudinal variation (Zachos

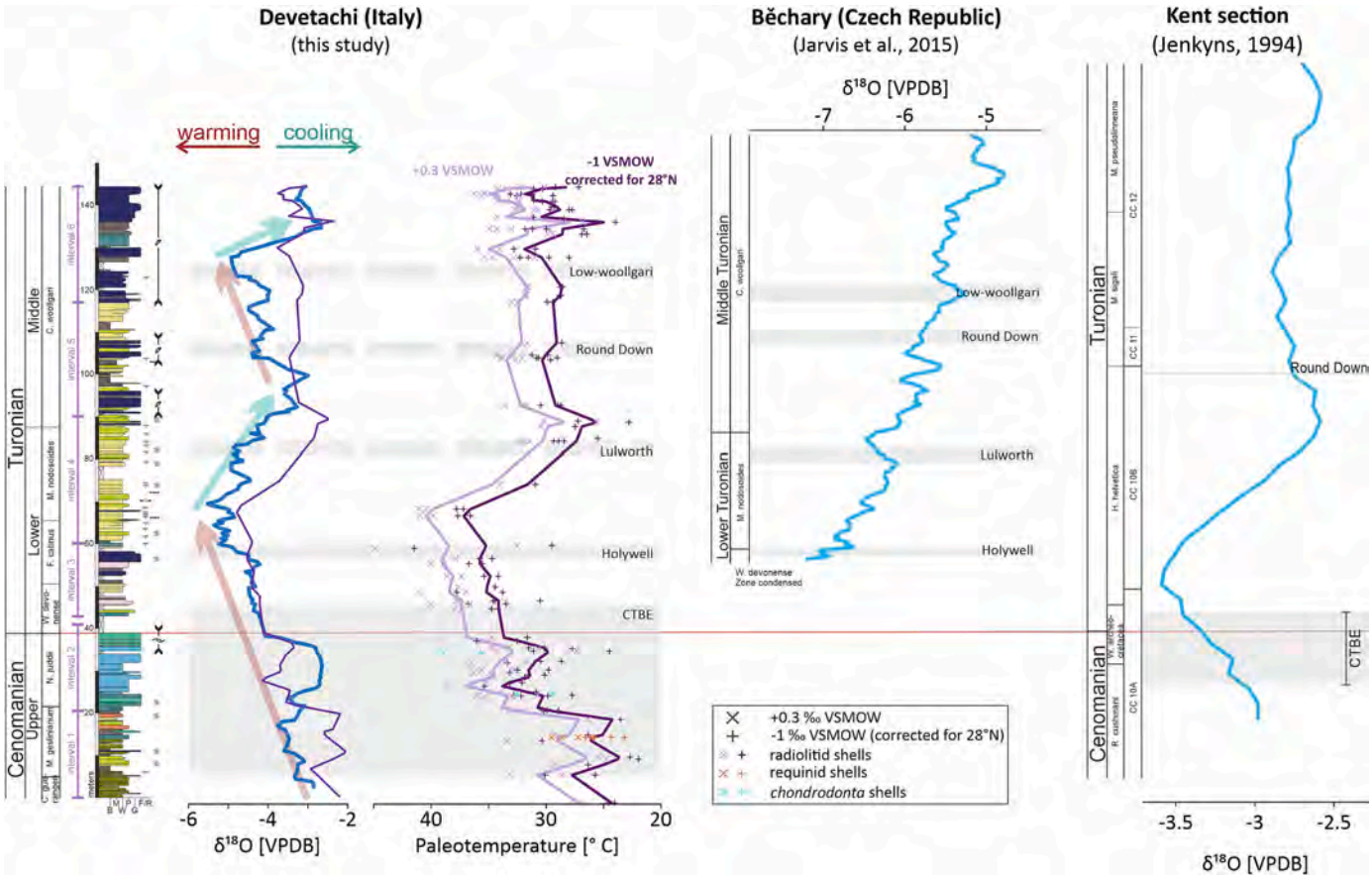

Fig. 8. Devetachi $\delta^{18}O$ and palaeotemperature curve compared with $\delta^{18}O$ profiles of pelagic sections from Běchary (Jarvis et al., 2015), and Kent sections (Jenkyns et al., 1994). Stratigraphic correlations are made according to the chronostratigraphy framework developed in Devetachi section. Palaeotemperature reconstruction is based on rudist shells following Anderson and Arthur (1983) equation, using a $\delta^{18}O_{seawater}$ of −1‰ corrected for palaeolatitude after Zachos et al. (1994) and a $\delta^{18}O_{seawater}$ of +0.3% modelled for the mid-Cretaceous western Tethyan ocean (Zhou et al., 2008). All pictured bulk rock $\delta^{18}O$ curves are smoothed (5 points moving average), and bivalve $\delta^{18}O$ and palaeotemperature curves are smoothed using LOESS fit (span 1.0).

et al., 1994). However, recent clumped isotope thermometry data and Cretaceous climate simulations have demonstrated that assuming a constant $\delta^{18}O_{seawater}$ value may not be valid in all the Cretaceous oceans (Dennis et al., 2013; Zhou et al., 2008; de Winter et al., 2021 among others). Using a global average $\delta^{18}O_{seawater}$ value would not consider either the spatial heterogeneity or different palaeoenvironmental settings in the Cretaceous water isotope signatures, which is also apparent in modern oceans (LeGrande and Schmidt, 2006). In shallow-marine settings, the oxygen isotopic composition of the water depends on the evaporation-precipitation balance and freshwater contribution (Dennis et al., 2013; Steuber, 1999; Steuber et al., 2005a). Modelled $\delta^{18}O_{seawater}$ suggests values between +0.3 and + 0.5 ‰ for the low- to mid-latitudes Tethyan surface waters in the Late Cretaceous (Zhou et al., 2008). Applying unrealistic $\delta^{18}O_{seawater}$ values leads to under- or over-estimations of the absolute palaeotemperatures. To account for these shortcomings, we calculated palaeotemperatures using two approaches: 1) An average $\delta^{18}O_{seawater}$ of −1 ‰ corrected for latitudinal changes (considering a palaeolatitude of 28°N for the studied section according to Barrier et al., 2018), using the equation of Zachos et al. (1994), and 2) A $\delta^{18}O_{seawater}$ value of +0.3 ‰ modelled for the western Tethys surface waters (Zhou et al., 2008). These assumptions might be over-simplifications as the $\delta^{18}O_{seawater}$ in Devetachi might have changed through the studied interval considering the alternations of more restricted and more open environmental conditions. According to these two "end-member" scenarios, the $\delta^{18}O$ data from Devetachi rudist shells suggest a temperature interval from 22 to 41 °C for scenario 1 and from 25 to 45 °C for scenario 2 (Fig. 8). The warmest derived palaeotemperatures >40 °C, coinciding with the lowest $\delta^{18}O$ values in the bulk rock data, are found in the Early Turonian. Such high temperatures would be most likely challenging for life (see discussion below) and this could imply that our lower temperature curve may be more realistic, at least for specific stratigraphic intervals. However, temperatures of >40 °C from low-latitude sites are also reconstructed by O'Brien et al. (2017) for the "hot" Early Turonian. Interestingly, the estimated temperatures during the CTBE/OAE-2 interval in Devetachi compare well with those calculated (31 to 37 °C) using the Tex_{86} proxy by Forster et al. (2007) from low-latitude ODP sites. Finally, middle Turonian cooling in Devetachi section is represented by an interval of minimum temperatures of 24 °C and 28 °C, considering scenarios 1 and 2 respectively, and maximum temperatures below 35 °C for both scenarios. These palaeotemperatures are similar to proposed middle–late Turonian maximum seasonal temperature changes of 24–35 °C (Walliser and Schöne, 2020) and 28–35 °C (Steuber et al., 2005a) considering $\delta^{18}O_{seawater}$ of −1 ‰. Furthermore, Walliser and Schöne (2020), using the modelled $\delta^{18}O_{seawater}$ of Zhou et al. (2008), calculated annual mean SSTs of 37 °C during the middle-late Turonian which is comparable with the maximum temperature for this interval in Devetachi section. Finally, palaeotemperatures of ~35 °C have been obtained using the Tex_{86}

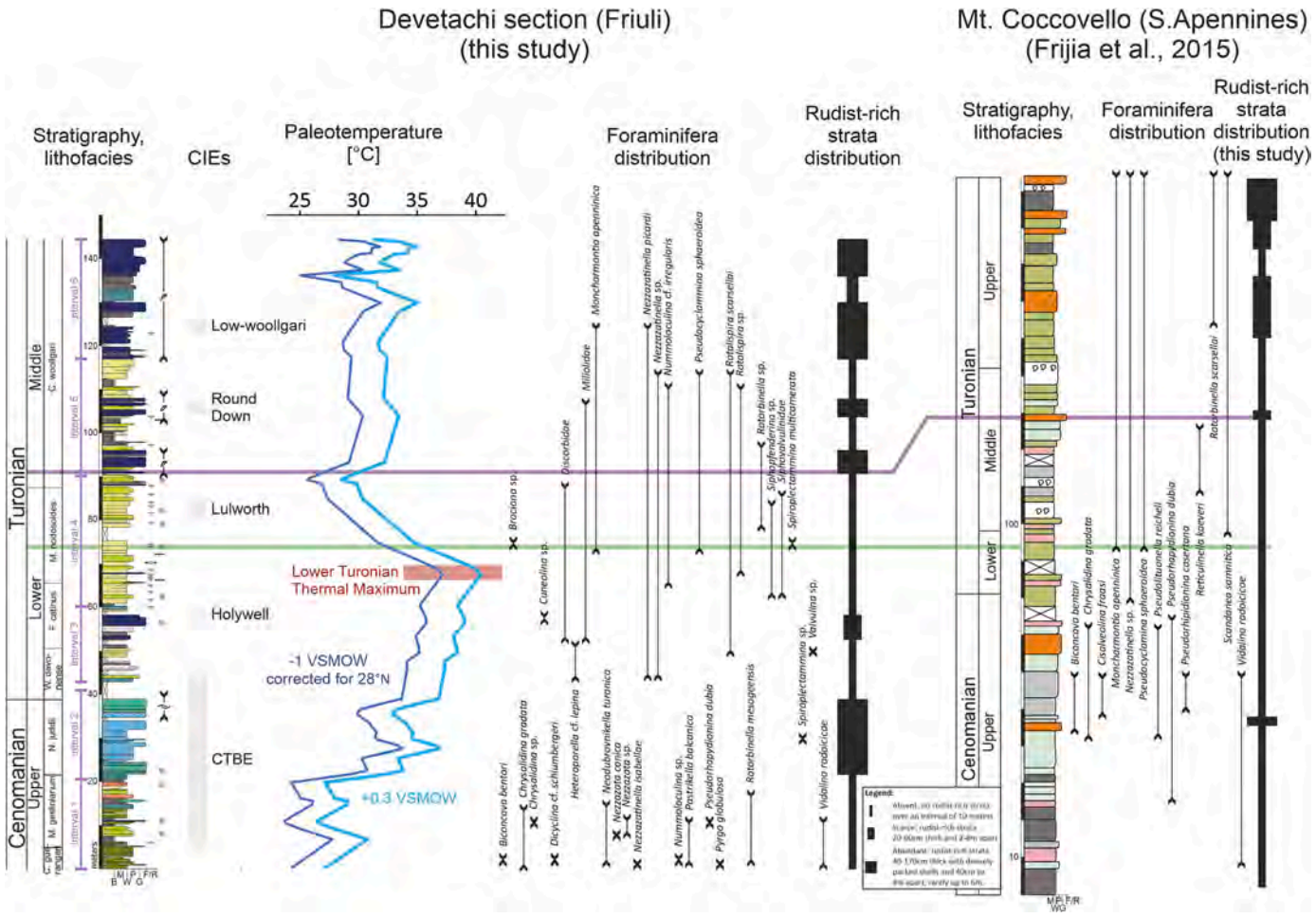

Fig. 9. Benthic foraminifera and rudists distribution in Devetachi section (Friuli Carbonate Platform, FCP) and Apennine carbonate platform (ACP, Frijia et al., 2015) across the upper Cenomanian-middle Turonian interval compared to the reconstructed temperature fluctuations. Foraminifera bioevents in the ACP are after Frijia et al. (2015). Black bars represent semiquantitative rudist abundance estimations (see text for details). Continuous green and purple lines mark the post-Cenomanian re-occurrence of high diversity foraminifera assemblages and rudist-dominated facies, respectively. Note that these bioevents occur after the Lower Turonian Thermal Maximum in both carbonate platform areas. (For interpretation of the references to colour in this figure legend, the reader is referred to the web version of this article.)

palaeothermometry from low palaeolatitude sites during the late Turonian-Early Coniacian interval (O'Brien et al., 2017).

5.4. Biota evolution and palaeotemperature changes

The high-resolution stratigraphic and geochemical framework developed in this study allows the evaluation of the possible impacts of palaeotemperatures on the distribution of benthic foraminifera and rudists in the FCP. The presented dataset (Devetachi) has been further enhanced by incorporating benthic foraminiferal stratigraphic distribution and semi-quantitative rudist abundance data from the ACP (see Frijia et al., 2014 and Frijia et al., 2015; Fig. 9).

The CTBE/OAE-2 dramatically impacted the shallow water fauna resulting in the extinction of several shallow marine groups (recent review in Steuber et al., 2023). Published data report a major crisis among the main Late Cretaceous shallow-water carbonate producers, such as benthic foraminifera (Parente et al., 2008) and rudist bivalves (e.g., Steuber et al., 2016; Steuber and Schlüter, 2012; Steuber et al., 2023 and reference therein). Structurally complex and high-diversity late Cenomanian benthic foraminifera assemblages with K-strategy lifestyles, such as alveolinids, orbitolinids, and soritids vanished slightly before the Cenomanian-Turonian boundary (Parente et al., 2008). The assemblage of small and morphologically simple r-strategist taxa that followed has been reported from resilient carbonate platforms of late-Cenomanian Early Turonian age (Parente et al., 2008; Arriaga et al., 2016; Consorti et al., 2021; Consorti and Schlagintweit, 2021). The CTBE/OAE-2 aftermath features the presence of these first newcomers, accompanied by smaller or structurally simple Cenomanian survivors such as the genera *Dicyclina* and *Rotorbinella* (Arriaga et al., 2016). These simple forms of small benthic foraminifera, however, established the foundations for the flourishment of late Cretaceous assemblages (Consorti et al., 2016; Schlagintweit and Yazdi-Moghadam, 2021; Yazdi-Moghadam and Schlagintweit, 2021).

The data from Devetachi section provide a similar picture of foraminifera distribution across the late Cenomanian-Turonian interval. The studied section shows the disappearance of larger Cenomanian foraminifera (*P. balcanica*, *C. gradata*, among others) at the onset of the CTBE/OAE-2. This bioevent is overlain by around 10 m of an interval barren of benthic foraminifera. An oligotypic foraminiferal association composed of small r-strategists such as miliolids, discorbidae, *Nezzazatinella picardi,* and *Siphopfenderina* sp. appears just above and continues for ~40 m. This assemblage correlates with the observed late Cenomanian to the Early Turonian warming, which culminates in the highest $\delta^{18}O$-based palaeotemperatures (Fig. 9). A more diverse benthic foraminifera association appears from meter 75 and it is characterized by some long-lasting Late Cretaceous benthic foraminifera taxa (Frijia et al., 2015; Velić, 2007): *Moncharmontia apenninica*, *Nezzazatinella* sp., *Pseudocyclammina sphaeroidea*, *Rotalispira* sp., *Rotorbinella* sp., *Rotalispira scarsellai*, *Braciana* sp., *Spiroplectammina* sp. and suggests the establishment of improved environmental conditions. The occurrence of this assemblage coincides with the onset of a cooling trend resulting in a temperature decrease of around 7 °C with respect to the warmest Lower Turonian peak. Frijia et al. (2015) and Arriaga et al. (2016) report a similar benthic foraminifera distribution from the ACP where r-strategist forms dominated during the uppermost Cenomanian-lower Turonian and the first occurrence of a more diversified assemblage including *M. apenninica* and *P. sphaeroidea* appeared from the middle/upper part of the Lower Turonian strata. The palaeotemperature reconstructions presented in this study suggest that the dramatic temperature increase across the CTBE/OAE-2, possibly in association with other palaeoenvironmental changes taking place during this event (review in Steuber et al., 2023), was harmful to the more specialized benthic foraminifera and that during the warmest Turonian interval only simple r-strategic forms could thrive. It was only when the temperatures cooled down below a threshold that benthic foraminifera started to diversify again.

The trend in rudists abundance is remarkably similar to that of the benthic foraminifera. The abundance of rudist-rich beds both in the FCP and in the ACP sharply decreases from the upper Cenomanian interval, becoming almost absent in the uppermost Cenomanian-lowermost Turonian strata, where only a few beds with rare and small rudist fragments are found. This pattern is seen in many locations around the world and represents a major drop in rudist communities and the extinction of several genera across the CTBE/OAE-2 (Johnson and Kauffman, 1990; Philip and Airaud-Crumiere, 1991). Rudists decline have been attributed to regional climate changes that may have caused less oxygen in neritic settings (Steuber and Löser, 2000) and to other environmental perturbations associated with the CTBE/OAE-2 (Steuber et al., 2023 and references therein). The rudists-poor interval in Devetachi coincides with the warmest phase indicated by the $\delta^{18}O$-based palaeotemperatures. Rudists-dominated strata reappear and become increasingly more abundant, in both the FCP and the ACP, in the middle Turonian where our data show a marked temperature decrease (Fig. 9, purple line).

Temperature is a critical factor limiting the ranges of most marine species, and thus influencing marine animals' evolution. Laboratory experiments and oceanographic studies show that marine organisms experience enhanced mortality rates when significant temperature increases/decreases exceed the upper/lower thermal limits for each species (Scotese et al., 2021 and reference therein). Maximum SST estimates obtained in this study are exceptionally warm indicating >40 °C in the Early Turonian. de Winter et al. (2021) also found similar temperature maxima in well-preserved Campanian rudists from Oman. These extreme values raise the question as to whether rudists and benthic foraminifera could tolerate such heat stress. Recent mollusks and foraminifera show a drastic increase in mortality in high-temperature conditions. Many modern organisms cannot survive when seawater temperatures exceed 40 °C (Garrabou et al., 2009 and references therein), though laboratory experiments and field observations on mollusks and foraminifera have proven that some species can live at temperatures as high as 40 °C (Song et al., 2014; Schmidt et al., 2016; Seuront et al., 2019). Finally, Veizer and Prokoph (2015) suggested preferred temperature ranges between 14 and 28 °C for fossil Phanerozoic bivalves. The ecological requirements of the studied rudists and foraminifera are difficult to assess and doing so is beyond the scope of this study. Furthermore, the reconstructed temperatures could have been biased by an incorrect assumption of the $\delta^{18}O_{seawater}$. Hence, more studies using different palaeotemperature proxies independent of $\delta^{18}O_{seawater}$ (e.g. clumped isotope analysis; de Winter et al., 2021) are required to further evaluate absolute palaeotemperatures.

However, the close match between the rudists and benthic foraminifera distribution and temperature fluctuations suggests a strong causal relationship. Song et al. (2014, 2021) proved a correlation between severe temperature changes and stratigraphic intervals of biodiversity loss. Temperature fluctuations with a magnitude of >5.2 °C and a rate > 10 °C/Ma seem to represent a critical threshold in determining mass extinction/biodiversity loss (Song et al., 2021). The data from Devetachi section record an increase of around 8–10 °C from the upper Cenomanian to the "hot" Lower Turonian in <1 Ma and a decrease of 7–9 °C until when diversified foraminifera assemblages and rudists-dominated facies reappear. Such results agree with the thresholds suggested by Song et al. (2021). We conclude that despite the possible co-occurring other environmental stressing factors (e.g., nutrient pulses, acidification episodes, anoxia; see review in Steuber et al., 2023), temperature played a major role in controlling the biota evolution in the late Cenomanian-Turonian shallow marine carbonate platforms.

6. Conclusions

In this study, a combined sedimentological, stratigraphic, and geochemical approach has been used to understand the evolution of the Friuli Carbonate Platform across the Cenomanian-Turonian, a critical

interval of the Late Cretaceous. A precise chronostratigraphic framework was developed using biostratigraphy together with $\delta^{13}C$ and $^{87}Sr/^{86}Sr$ stratigraphy which constrained the studied section to the upper Cenomanian-middle Turonian interval.

Using $\delta^{18}O$ analysis on well-preserved bulk rock and rudist shells enabled us to build high-resolution palaeotemperature curves and to estimate palaeotemperature minima and maxima. The results suggest a close match in temperature evolution between Devetachi section and SSTs reconstructed from open ocean sites, showing marked warming from the late Cenomanian to the Early Turonian and a subsequent cooling phase. In the studied section, the Early Turonian warmest interval temperatures reached as high as 41–45 °C, marking the timing of the KTM in the peri-Adriatic area. Palaeontological data show that benthic foraminifera and rudists distribution follows palaeotemperature fluctuations; they were severely impacted during the KTM and took-up again in the cooler late early/middle Turonian. The close match between the biotic record in the Friuli Carbonate Platform and the Apennine Carbonate Platform (1000 km away) suggests the major controlling role of temperature in the evolution of Late Cretaceous carbonate platforms. However, further studies from different carbonate neritic successions around the world and a multidisciplinary methodology are required to substantiate this hypothesis and infer the causal relationships between different environmental factors and biota evolutionary trends.

CRediT authorship contribution statement

B. Křížová: Writing – review & editing, Writing – original draft, Investigation, Formal analysis, Data curation, Conceptualization. **L. Consorti:** Writing – original draft, Formal analysis. **S. Cardelli:** Investigation, Formal analysis. **K.E. Schmitt:** Writing – review & editing, Formal analysis, Data curation. **V. Brombin:** Formal analysis, Data curation. **M. Franceschi:** Writing – original draft. **G. Tunis:** Investigation, Data curation. **L. Bonini:** Writing – original draft. **G. Frijia:** Writing – review & editing, Writing – original draft, Validation, Supervision, Project administration, Investigation, Funding acquisition, Data curation, Conceptualization.

Declaration of Competing Interest

The authors declare that they have no known competing financial interests or personal relationships that could have appeared to influence the work reported in this paper.

Data availability

Data will be made available on request.

Acknowledgments

Support for this work was provided by a UNIFE research grant FIR 2019 to GF and by a SEPM research grant to BK. We are grateful to Sylvia Riechelmann from the Institut für Geologie, Mineralogie und Geophysik (Ruhr- Universität, Bochum) for taking care of the Sr-isotope analyses and to Christopher Toland (Oolithica Geoscience) for reading a revised version of the manuscript. Finally, the manuscript benefited greatly from the criticism and suggestions of two anonymous reviewers and the careful and patient editorial work of Alex Dickson.

Appendix A. Supplementary data

Supplementary data to this article can be found online at https://doi.org/10.1016/j.palaeo.2023.111995.

References

Allan, J.R., Matthews, R.K., 1982. Isotope signatures associated with early meteoric diagenesis. Sedimentology 29, 797–817. https://doi.org/10.1111/j.1365-3091.1982.tb00085.x.

Anderson, T.F., Arthur, M.A., 1983. Stable isotopes of oxygen and carbon and their application to sedimentologic and paleoenvironmental problems. In: Stable Isotopes in Sedimentary Geology, SEPM Short Course No. 10, 10. SEPM, pp. 1–151.

Arriaga, M., Frijia, G., Parente, M., Caus, E., 2016. Benthic foraminifera in the aftermath of the Cenomanian-Turonian boundary extinction event in the carbonate platform facies of the southern Apennines (Italy). J. Foraminiferal Res. 46, 9–24.

Barrier, E., Vrielynck, J., Brouillet, J.F., Brunet, M.F., 2018. Atlas DARIUS PDF - Paleotectonic Reconstruction of the Central Tethyan Realm.

Bice, K.L., Birgel, D., Meyers, P.A., Dahl, K.A., Hinrichs, K.-U., Norris, R.D., 2006. A multiple proxy and model study of Cretaceous upper ocean temperatures and atmospheric CO 2 concentrations: CRETACEOUS MULTIPLE PROXY STUDY. Paleoceanography 21. https://doi.org/10.1029/2005PA001203 n/a-n/a.

Boix, C., Frijia, G., Vicedo, V., Bernaus, J.M., Di Lucia, M., Parente, M., Caus, E., 2011. Larger foraminifera distribution and strontium isotope stratigraphy of the La Cova limestones (Coniacian–Santonian, "Serra del Montsec", Pyrenees, NE Spain). Cretac. Res. 32, 806–822. https://doi.org/10.1016/j.cretres.2011.05.009.

Bornemann, A., Norris, R.D., Friedrich, O., Beckmann, B., Schouten, S., Damsté, J.S.S., Vogel, J., Hofmann, P., Wagner, T., 2008. Isotopic evidence for Glaciation during the Cretaceous Supergreenhouse. Science 319, 189–192. https://doi.org/10.1126/science.1148777.

Burgener, L., Hyland, E., Reich, B.J., Scotese, C., 2023. Cretaceous climates: Mapping paleo-Köppen climatic zones using a Bayesian statistical analysis of lithologic, paleontologic, and geochemical proxies. Palaeogeogr. Palaeoclimatol. Palaeoecol. 613, 111373 https://doi.org/10.1016/j.palaeo.2022.111373.

Chiocchini, M., Pampaloni, M.L., Pichezzi, R.M., 2012. Microfacies and microfossils of the Mesozoic carbonate successions of Latium and Abruzzi (Central Italy). In: Memorie per Servire alla Descrizione della Carta Geologica D'Italia, ISPRA, 17. Dipartimento Difesa del Suolo, pp. 1–269.

Clarke, L.J., Jenkyns, H.C., 1999. New oxygen isotope evidence for long-term Cretaceous climatic change in the Southern Hemisphere. Geol 27, 699. https://doi.org/10.1130/0091-7613(1999)027<0699:NOIEFL>2.3.CO;2.

Consorti, L., Schlagintweit, F., 2021. A new Vandenbroeckia Marie, 1958 (Peneroplidae) adds further data on the survival of shallow-water benthic Foraminifera through the Cenomanian-Turonian boundary. Cretac. Res. 126, 104910 https://doi.org/10.1016/j.cretres.2021.104910.

Consorti, L., Boix, C., Caus, E., 2016. Pseudorhapydionina bilottei sp. nov., an endemic foraminifera from the post-Cenomanian/Turonian boundary (Pyrenees, NE Spain). Cretac. Res. 59, 147–154. https://doi.org/10.1016/j.cretres.2015.10.021.

Consorti, L., Arbulla, D., Bonini, L., Fabbi, S., Fanti, F., Franceschi, M., Frijia, G., Pini, G. A., 2021. The Mesozoic palaeoenvironmental richness of the Trieste Karst, 13. GFT, pp. 1–40. https://doi.org/10.3301/GFT.2021.06.

Cramer, B.D., Jarvis, I., 2020. Carbon isotope stratigraphy. In: Geologic Time Scale 2020. Elsevier, pp. 309–343. https://doi.org/10.1016/B978-0-12-824360-2.00011-5.

Del Viscio, G., Morsilli, M., Posenato, R., Frijia, G., Moro, A., Mezga, A., 2022. Proliferation of Chondrodonta in upper Cenomanian shallow-water limestones of the Adriatic Carbonate Platform (Croatia) as a proxy of environmental instability. Cretac. Res. 134, 105151 https://doi.org/10.1016/j.cretres.2022.105151.

Dennis, K.J., Cochran, J.K., Landman, N.H., Schrag, D.P., 2013. The climate of the late Cretaceous: New insights from the application of the carbonate clumped isotope thermometer to Western Interior Seaway macrofossil. Earth Planet. Sci. Lett. 362, 51–65. https://doi.org/10.1016/j.epsl.2012.11.036.

Flügel, E., 2004. Microfacies of Carbonate Rocks: Analysis, Interpretation and Application. Springer, Berlin, New York.

Forster, A., Schouten, S., Moriya, K., Wilson, P.A., Sinninghe Damsté, J.S., 2007. Tropical warming and intermittent cooling during the Cenomanian/Turonian oceanic anoxic event 2: Sea surface temperature records from the equatorial Atlantic: TROPICAL CENOMANIAN/TURONIAN SST RECORDS. Paleoceanography 22. https://doi.org/10.1029/2006PA001349 n/a-n/a.

Friedrich, O., Norris, R.D., Erbacher, J., 2012. Evolution of middle to late Cretaceous oceans—a 55 m.y. record of Earth's temperature and carbon cycle. Geology 40, 107–110. https://doi.org/10.1130/G32701.1.

Frijia, G., 2006. Stratigrafia integrata (bio- e chemostratigrafia) nelle successioni carbonatiche di mare basso del Cretacico Superiore dell'Appennino meridionale. Unpublished PhD thesis, 200 pp. University of Naples, Italy.

Frijia, G., Parente, M., 2008a. Strontium isotope stratigraphy in the upper Cenomanian shallow-water carbonates of the southern Apennines: short-term perturbations of marine 87Sr/86Sr during the oceanic anoxic event 2. Palaeogeogr. Palaeoclimatol. Palaeoecol. 261, 15–29. https://doi.org/10.1016/j.palaeo.2008.01.003.

Frijia, G., Parente, M., 2008b. Reticulinella kaeveri CHERCHI, RADOIC IĆ & SCHROEDER: a marker for the middle-upper Turonian in the shallow-water carbonate facies of the peri-Adriatic area. Bull. Soc. Geol. Ital. (Ital. J. Geosci.) 127 (2), 275–284.

Frijia, G., Parente, M., Mutti, M., 2014. The distribution of rudist-rich beds in the Upper Cretaceous of the Apennine Carbonate Platform (southern Italy): just a local pattern?. In: Abstract Book of the Tenth International Congress on Rudist Bivalves, Bellaterra, Spain.

Frijia, G., Parente, M., Di Lucia, M., Mutti, M., 2015. Carbon and strontium isotope stratigraphy of the Upper Cretaceous (Cenomanian-Campanian) shallow-water carbonates of southern Italy: Chronostratigraphic calibration of larger foraminifera biostratigraphy. Cretac. Res. 53, 110–139. https://doi.org/10.1016/j.cretres.2014.11.002.

Frijia, G., Forkner, R., Minisini, D., Pacton, M., Struck, U., Mutti, M., 2019. Cyanobacteria Proliferation in the Cenomanian-Turonian Boundary Interval of the Apennine Carbonate Platform: Immediate Response to the Environmental Perturbations Associated with OAE-2? Geochem. Geophys. Geosyst. 20, 2698–2716. https://doi.org/10.1029/2019GC008306.

Galeotti, S., Rusciadelli, G., Sprovieri, M., Lanci, L., Gaudio, A., Pekar, S., 2009. Sea-level control on facies architecture in the Cenomanian–Coniacian Apulian margin (Western Tethys): A record of glacio-eustatic fluctuations during the Cretaceous greenhouse? Palaeogeogr. Palaeoclimatol. Palaeoecol. 276, 196–205. https://doi.org/10.1016/j.palaeo.2009.03.011.

Garrabou, J., Coma, R., Bensoussan, N., Bally, M., Chevaldonné, P., Cigliano, M., Diaz, D., Harmelin, J.G., Gambi, M.C., Kersting, D.K., Ledoux, J.B., Lejeusne, C., Linares, C., Marschal, C., Pérez, T., Ribes, M., Romano, J.C., Serrano, E., Teixido, N., Torrents, O., Zabala, M., Zuberer, F., Cerrano, C., 2009. Mass mortality in Northwestern Mediterranean rocky benthic communities: effects of the 2003 heat wave. Glob. Chang. Biol. 15, 1090–1103. https://doi.org/10.1111/j.1365-2486.2008.01823.x.

Gradstein, F.M., Ogg, J.G., Schmitz, M.D., Ogg, G.M. (Eds.), 2020. Geologic Time Scale 2020. Elsevier.

Grossman, E.L., 2012. Applying Oxygen Isotope Paleothermometry in Deep Time. Paleontol. Soc. Pap. 18, 39–68. https://doi.org/10.1017/S1089332600002540.

Grotzinger, J.P., Fike, D.A., Fischer, W.W., 2011. Enigmatic origin of the largest-known carbon isotope excursion in Earth's history. Nat. Geosci. 4, 285–292. https://doi.org/10.1038/ngeo1138.

Haq, B.U., 2014. Cretaceous eustasy revisited. Glob. Planet. Chang. 113, 44–58. https://doi.org/10.1016/j.gloplacha.2013.12.007.

Hay, W.W., 2008. Evolving ideas about the Cretaceous climate and ocean circulation. Cretac. Res. 29, 725–753. https://doi.org/10.1016/j.cretres.2008.05.025.

Hay, W.W., Floegel, S., 2012. New thoughts about the Cretaceous climate and oceans. Earth Sci. Rev. 115, 262–272. https://doi.org/10.1016/j.earscirev.2012.09.008.

Huber, B.T., Norris, R.D., MacLeod, K.G., 2002. Deep-sea paleotemperature record of extreme warmth during the Cretaceous. Geoloy 30, 123. https://doi.org/10.1130/0091-7613(2002)030<0123:DSPROE>2.0.CO;2.

Huber, B.T., MacLeod, K.G., Watkins, D.K., Coffin, M.F., 2018. The rise and fall of the Cretaceous Hot Greenhouse climate. Glob. Planet. Chang. 167, 1–23. https://doi.org/10.1016/j.gloplacha.2018.04.004.

Huck, S., Heimhofer, U., 2015. Improving shallow-water carbonate chemostratigraphy by means of RUDIST BIVALVE sclerochemistry: RUDIST BIVALVE CHEMOSTRATIGRAPHY. Geochem. Geophys. Geosyst. 16, 3111–3128. https://doi.org/10.1002/2015GC005988.

Huck, S., Heimhofer, U., 2021. Early Cretaceous sea surface temperature evolution in subtropical shallow seas. Sci. Rep. 11, 19765. https://doi.org/10.1038/s41598-021-99094-2.

Jarvis, I., Trabucho-Alexandre, J., Gröcke, D.R., Uličný, D., Laurin, J., 2015. Intercontinental correlation of organic carbon and carbonate stable isotope records: evidence of climate and sea-level change during the Turonian (Cretaceous). Deposit. Rec. 1, 53–90. https://doi.org/10.1002/dep2.6.

Jenkyns, H.C., Gale, A.S., Corfield, R.M., 1994. Carbon- and oxygen-isotope stratigraphy of the English Chalk and Italian Scaglia and its palaeoclimatic significance. Geol. Mag. 131, 1–34. https://doi.org/10.1017/S0016756800010451.

Johnson, C.C., Kauffman, E.G., 1990. Originations, radiations and extinctions of Cretaceous rudistid bivalve species in the Caribbean Province. In: Kauffman, Erle G., Walliser, O.H. (Eds.), Extinction Events in Earth History, Lecture Notes in Earth Sciences. Springer-Verlag, Berlin/Heidelberg, pp. 305–324. https://doi.org/10.1007/BFb0011154.

Jurkovšek, B., Biolchi, S., Furlani, S., Kolar-Jurkovšek, T., Zini, L., Jež, J., Tunis, G., Bavec, M., Cucchi, F., 2016. Geology of the Classical Karst Region (SW Slovenia–NE Italy). J. Maps 12, 352–362. https://doi.org/10.1080/17445647.2016.1215941.

LeGrande, A.N., Schmidt, G.A., 2006. Global gridded data set of the oxygen isotopic composition in seawater. Geophys. Res. Lett. 33, L12604. https://doi.org/10.1029/2006GL026011.

Lohmann, K.C., 1988. Geochemical patterns of meteoric diagenetic systems and their application to studies of Paleokarst. In: James, N.P., Choquette, P.W. (Eds.), Paleokarst. Springer, New York, New York, NY, pp. 58–80. https://doi.org/10.1007/978-1-4612-3748-8_3.

MacLeod, K.G., Huber, B.T., Berrocoso, Á.J., Wendler, I., 2013. A stable and hot Turonian without glacial δ18O excursions is indicated by exquisitely preserved Tanzanian foraminifera. Geology 41, 1083–1086. https://doi.org/10.1130/G34510.1.

Marshall, J., 1992. Climatic and oceanographic isotopic signals from the carbonate rock record and their preservation. Geol. Mag. 129, 143–160.

McArthur, J.M., 1994. Recent trends in strontium isotope stratigraphy. Terra Nova 6, 331–358. https://doi.org/10.1111/j.1365-3121.1994.tb00507.x.

McArthur, J.M., Horwath, R.J., 2020. Strontium Isotope Stratigraphy: Lowess Version 6: Best-Fit to the Marine Sr-Isotope Curve for 0 to 509 ma and Accompanying Look-Up Table for Deriving Numerical Age.

Melis, R., Colizza, E., Pugliese, N., 2000. Eventi cenomaniani e turoniani nell'abisso di Trebiciano (Carso triestino). Accad. Naz. Sci. Lett. Arti Modena Collana Studi 21, 169–176.

Miller, K.G., Sugarman, P.J., Browning, J.V., Kominz, M.A., Olsson, R.K., Feigenson, M. D., Hernández, J.C., 2004. Upper Cretaceous sequences and sea-level history, New Jersey Coastal Plain. Geo. Soc. Am. Bull. 116, 368. https://doi.org/10.1130/B25279.1.

Mueller, M., Igbokwe, O.A., Walter, B., Pederson, C.L., Riechelmann, S., Richter, D.K., Albert, R., Gerdes, A., Buhl, D., Neuser, R.D., Bertotti, G., Immenhauser, A., 2020. Testing the preservation potential of early diagenetic dolomites as geochemical archives. Sedimentology 67 (2), 849–881. https://doi.org/10.1111/sed.1266.

O'Brien, C.L., Robinson, S.A., Pancost, R.D., Sinninghe Damsté, J.S., Schouten, S., Lunt, D.J., Alsenz, H., Bornemann, A., Bottini, C., Brassell, S.C., Farnsworth, A., Forster, A., Huber, B.T., Inglis, G.N., Jenkyns, H.C., Linnert, C., Littler, K., Markwick, P., McAnena, A., Mutterlose, J., Naafs, B.D.A., Püttmann, W., Sluijs, A., van Helmond, N.A.G.M., Vellekoop, J., Wagner, T., Wrobel, N.E., 2017. Cretaceous sea-surface temperature evolution: Constraints from TEX86 and planktonic foraminiferal oxygen isotopes. Earth Sci. Rev. 172, 224–247. https://doi.org/10.1016/j.earscirev.2017.07.012.

O'Connor, L.K., Robinson, S.A., Naafs, B.D.A., Jenkyns, H.C., Henson, S., Clarke, M., Pancost, R.D., 2019. Late Cretaceous Temperature Evolution of the Southern High Latitudes: a TEX $_{86}$ Perspective. Paleoceanogr. Paleoclimatol. 34, 436–454. https://doi.org/10.1029/2018PA003546.

Oehlert, A.M., Swart, P.K., 2019. Rolling window regression of δ 13C and δ18O values in carbonate sediments: Implications for source and diagenesis. Deposit. Rec. 5, 613–630. https://doi.org/10.1002/dep2.88.

Otoničar, B., 2007. Upper Cretaceous to Paleogene forbulge unconformity associated with foreland basin evolution (Kras, Matarsko podolje and Istria; SW Slovenia and NW Croatia). Acta Carsol. 36, 101–120.

Parente, M., Frijia, G., Di Lucia, M., Jenkyns, H.C., Woodfine, R.G., Baroncini, F., 2008. Stepwise extinction of larger foraminifers at the Cenomanian/Turonian: a shallow-water perspective on nutrient fluctuations during Oceanic Anoxic Event 2 (Bonarelli Event). Geology 39, 715–718.

Paul, C.R.C., Lamolda, M.A., Mitchell, S.F., Vaziri, M.R., Gorostidi, A., Marshall, J.D., 1999. The Cenomanian-Turonian boundary at Eastbourne (Sussex, UK): a proposed European reference section. Palaeogeogr. Palaeoclimatol. Palaeoecol. 150, 83–121.

Petrizzo, M.R., Amaglio, G., Watkins, D.K., MacLeod, K.G., Huber, B.T., Hasegawa, T., Wolfgring, E., 2022. Biotic and Paleoceanographic changes across the late Cretaceous Oceanic Anoxic Event 2 in the Southern High Latitudes (IODP Sites U1513 and U1516, SE Indian Ocean). Paleoceanog. Paleoclimatol. 37 https://doi.org/10.1029/2022PA004474.

Philip, J.M., Airaud-Crumiere, C., 1991. The demise of the rudist-bearing carbonate platforms at the Cenomanian/Turonian boundary: a global control. Coral Reefs 10, 115–125.

Picotti, V., Cobianchi, M., Luciani, V., Blattmann, F., Schenker, T., Mariani, E., Bernasconi, S.M., Weissert, H., 2019. Change from rimmed to ramp platform forced by regional and global events in the Cretaceous of the Friuli-Adriatic Platform (Southern Alps, Italy). Cretac. Res. 104, 104177 https://doi.org/10.1016/j.cretres.2019.07.007.

Pohl, A., Laugié, M., Borgomano, J., Michel, J., Lanteaume, C., Scotese, C.R., Frau, C., Poli, E., Donnadieu, Y., 2019. Quantifying the paleogeographic driver of Cretaceous carbonate platform development using paleoecological niche modeling. Palaeogeogr. Palaeoclimatol. Palaeoecol. 514, 222–232. https://doi.org/10.1016/j.palaeo.2018.10.017.

Pucéat, E., Lécuyer, C., Donnadieu, Y., Naveau, P., Cappetta, H., Ramstein, G., Huber, B. T., Kriwet, J., 2007. Fish tooth δ18O revising late Cretaceous meridional upper ocean water temperature gradients. Geology 35, 107. https://doi.org/10.1130/G23103A.1.

Sanders, D., 2001. Burrow-mediated carbonate dissolution in rudist biostromes (Aurisina, Italy): implications for taphonomy in tropical, shallow subtidal carbonate environments. Palaeogeogr. Palaeoclimatol. Palaeoecol. 168, 39–74. https://doi.org/10.1016/S0031-0182(00)00249-2.

Schlagintweit, F., Yazdi-Moghadam, M., 2021. *Moncharmontia* De Castro 1967, benthic foraminifera from the middle-upper Cenomanian of the Sarvak Formation of SW Iran (Zagros Zone): a CTB survivor taxon. Mar. Micropaleontol. 67, 19–29. https://doi.org/10.47894/mpal.67.1.03.

Schmidt, C., Titelboim, D., Brandt, J., Herut, B., Abramovich, S., Almogi-Labin, A., Kucera, M., 2016. Extremely heat tolerant photo-symbiosis in a shallow marine benthic foraminifera. Sci. Rep. 6, 30930. https://doi.org/10.1038/srep30930.

Schmitt, K.E., Huck, S., Krummacker, M., De Winter, N.J., Godet, A., Claeys, P., Heimhofer, U., 2022. Radiolitid rudists: an underestimated archive for Cretaceous climate reconstruction? Lethaia 55, 1–21. https://doi.org/10.18261/let.55.4.4.

Schroeder, R., Neumann, M. (Eds.), 1985. Les grands foraminiféres du Crétacé moyen de la région méditerraniénne. Geobios Mém. Spec.

Scotese, C.R., Song, H., Mills, B.J.W., van der Meer, D.G., 2021. Phanerozoic paleotemperatures: the earth's changing climate during the last 540 million years. Earth Sci. Rev. 215, 103503 https://doi.org/10.1016/j.earscirev.2021.103503.

Seuront, L., Nicastro, K.R., Zardi, G.I., Goberville, E., 2019. Decreased thermal tolerance under recurrent heat stress conditions explains summer mass mortality of the blue mussel Mytilus edulis. Sci. Rep. 9, 17498. https://doi.org/10.1038/s41598-019-53580-w.

Song, H., Wignall, P., Chu, D., Tong, J., Sun, Y., Song, H., He, W., Tian, L., 2014. Anoxia/high temperature double whammy during the Permian-Triassic marine crisis and its aftermath. Sci. Rep. 4, 4132. https://doi.org/10.1038/srep04132.

Song, Haijun, Wignall, P.B., Song, Huyue, Dai, X., Daoliang, C., 2019. Seawater temperature and dissolved oxygen over the past 500 million years. J. Earth Sci. 30, 236–243. https://doi.org/10.1007/s12583-018-1002-2.

Song, Haijun, Kemp, D.B., Tian, L., Chu, D., Song, Huyue, Dai, X., 2021. Thresholds of temperature change for mass extinctions. Nat. Commun. 12, 4694. https://doi.org/10.1038/s41467-021-25019-2.

Steuber, T., 1999. Isotopic and chemical intra-shell variations in low-Mg calcite of rudist bivalves (Mollusca-Hippuritacea): disequilibrium fractionations and late Cretaceous seasonality. Int. J. Earth Sci. 88, 551–570. https://doi.org/10.1007/s005310050284.

Steuber, T., 2003. Strontium isotope stratigraphy of Cretaceous hippuritid rudist bivalves: rates of morphological change and heterochronic evolution. Palaeogeogr.

Palaeoclimatol. Palaeoecol. 200, 221–243. https://doi.org/10.1016/S0031-0182(03)00452-8.

Steuber, T., Löser, H., 2000. Species richness and abundance patterns of Tethyan Cretaceous rudist bivalves (Mollusca; Hippuritacea) in the Central-Eastern Mediterranean and Middle East, analysed from a paleontological database. Palaeogeogr. Paleoclimatol. Palaeoecol. 162, 75–104. Database located at. http://www.ruhr-uni-bochum.de/sediment/rudinet/intro.htm.

Steuber, T., Schlüter, M., 2012. Strontium-isotope stratigraphy of Upper Cretaceous rudist bivalves: Biozones, evolutionary patterns and sea-level change calibrated to numerical ages. Earth Sci. Rev. 114, 42–60. https://doi.org/10.1016/j.earscirev.2012.04.004.

Steuber, T., Rauch, M., Masse, J.-P., Graaf, J., Malkoč, M., 2005a. Low-latitude seasonality of Cretaceous temperatures in warm and cold episodes. Nature 437, 1341–1344. https://doi.org/10.1038/nature04096.

Steuber, T., Korbar, T., Jelaska, V., Gusic, I., 2005b. Strontium isotope stratigraphy of Upper Cretaceous platform carbonates of the island of Brac (Adriatic Sea, Croatia): implications for global correlation of platform evolution and biostratigraphy. Cretac. Res. 26, 741–756.

Steuber, T., Scott, R.W., Mitchell, S.F., Skelton, P.W., 2016. Stratigraphy and Diversity Dynamics of Jurassic–Cretaceous Hippuritida (Rudist Bivalves). Treatise online, Part N 1.

Steuber, T., Löser, H., Mutterlose, J., Parente, M., 2023. Biogeodynamics of Cretaceous marine carbonate production. Earth Sci. Rev. 238, 104341 https://doi.org/10.1016/j.earscirev.2023.104341.

Swart, P.K., Oehlert, A.M., 2018. Revised interpretations of stable C and O patterns in carbonate rocks resulting from meteoric diagenesis. Sediment. Geol. 364, 14–23. https://doi.org/10.1016/j.sedgeo.2017.12.005.

Tsikos, H., Jenkyns, H.C., Walsworth-Bell, B., Petrizzo, M.R., Forster, A., Kolonic, S., 2004. Carbon-isotope stratigraphy recorded by the Cenomanian-Turonian Oceanic Anoxic Event: Correlation and implications based on three key localities. J. Geol. Soc. Lond. 161, 711–719.

Veizer, J., Prokoph, A., 2015. Temperatures and oxygen isotopic composition of Phanerozoic oceans. Earth Sci. Rev. 146, 92–104. https://doi.org/10.1016/j.earscirev.2015.03.008.

Velić, I., 2007. Stratigraphy and Palaeobiogeography of Mesozoic Benthic Foraminifera of the Karst Dinarides (SE Europe). Geol. Croat. 60, 1–113.

Vlahović, I., Tišljar, J., Velić, I., Matičec, D., 2005. Evolution of the Adriatic Carbonate Platform: Palaeogeography, main events and depositional dynamics. Palaeogeogr. Palaeoclimatol. Palaeoecol. 220, 333–360. https://doi.org/10.1016/j.palaeo.2005.01.011.

Walliser, E.O., Schöne, B.R., 2020. Paleoceanography of the late Cretaceous northwestern Tethys Ocean: Seasonal upwelling or steady thermocline? PLoS One 15, e0238040. https://doi.org/10.1371/journal.pone.0238040.

de Winter, N.J., Müller, I.A., Kocken, I.J., Thibault, N., Ullmann, C.V., Farnsworth, A., Lunt, D.J., Claeys, P., Ziegler, M., 2021. Absolute seasonal temperature estimates from clumped isotopes in bivalve shells suggest warm and variable greenhouse climate. Commun. Earth Environ. 2, 121. https://doi.org/10.1038/s43247-021-00193-9.

Yazdi-Moghadam, M., Schlagintweit, F., 2021. Cenomanian "orbitoliniform" foraminifera—State of the art and description of *Ebrahimiella dercourti* (Decrouez and Moullade, 1974) gen. et comb. nov (family Coskinolinidae) from the Sarvak Formation (SW Iran, Zagros Zone). Cretac. Res. 126, 104885. https://doi.org/10.1016/j.cretres.2021.104885.

Zachos, J.C., Stott, L.D., Lohmann, K.C., 1994. Evolution of early Cenozoic marine temperatures. Paleoceanography 9, 353–387. https://doi.org/10.1029/93PA03266.

Zhou, J., Poulsen, C.J., Pollard, D., White, T.S., 2008. Simulation of modern and middle Cretaceous marine δ^{18}O with an ocean-atmosphere general circulation model: MODERN, MID-CRETACEOUS SEAWATER δ^{18}O. Paleoceanography 23. https://doi.org/10.1029/2008PA001596 n/a-n/a.